Supporting Information

Anomalous Dynamics of in Vivo Cargo Delivery by Motor Protein Multiplexes

Kyujin Shin[†a], Sanggeun Song[†b,c,d], Yo Han Song[†a], Seungsoo Hahn[b,e], Ji-Hyun Kim[b], Gibok Lee[a], In-Chun Jeong[b,c,d], Jaeyoung Sung*[b,c,d], and Kang Taek Lee*[a]

[a]Department of Chemistry, School of Physics and Chemistry, Gwangju Institute of Science and Technology (GIST), Gwangju, 61005, Korea.
[b]Creative Research Initiative Center for Chemical Dynamics in Living Cells, Chung-Ang University, Seoul, 06974, Korea.
[c]Department of Chemistry, Chung-Ang University, Seoul, 06974, Korea.
[d]National Institute of Innovative Functional Imaging, Chung-Ang University, Seoul, 06974, Korea.
[e]Da Vinci College of General Education, Chung-Ang University, Seoul, 06974, Korea.

† These authors contributed equally to this work.
* Correspondence and requests for materials should be addressed to J.S. (email: jaeyoung@cau.ac.kr) and K.T.L. (email: ktlee@gist.ac.kr).

This PDF file includes:

Other Supplemental Material for this manuscript include the following:

Movies S1 and S2

Supplementary Method 1 | Materials and Methods

General methods. To increase the field of view, we employed a wide-field epi-fluorescence microscopy capable of scanning the objective lens along the z-axis (Figures. S1A and S11)[1]. The signal from every UCNP between these two planes can be detected, which is advantageous over conventional techniques where movements of fluorescent probes out of one objective focal plane cause signal disappearance. The UCNP coordinates were determined by a Gaussian point-spread function[2, 3]. With this double-plane imaging, the mean trajectory length is estimated to be 70–120 seconds for our system (Figure S12).

Chemicals. Yttrium (III) acetate hydrate (99.9 %), ytterbium (III) acetate tetrahydrate (99.9 %), erbium (III) acetate hydrate (99.9 %), 1-octadecene (technical grade, 90 %), oleic acid (technical grade, 90 %), ammonium fluoride (≥ 98 %), and sodium hydroxide (≥ 98 %) were purchased from Sigma-Aldrich. 1,2- dipalmitoyl-sn-glycero-3-phosphoethanolamine-N-[methoxy(polyethylene glycol)-2000] (mPEG) and 1,2-distearoyl-sn-glycero-3-phosphoethanolamine-N-[amino(polyethylene glycol)-2000] (DSPE-PEG-NH_2) were sourced from Avanti Polar Lipids, Inc. The other reagents and organic solvents used were of sufficient quality and grade. All chemical reagents were used without further purification.

Preparation of PEG-Phospholipid functionalized UCNPs (β-$NaYF_4$: 20 mol% Yb^{3+}, 2 mol% Er^{3+}). The β-$NaYF_4$: Yb^{3+}, Er^{3+} UCNPs were synthesized as previously reported with minor modification[4]. $Y(CH_3COO)_3 \cdot xH_2O$ (0.78 mmol), $Yb(CH_3COO)_3 \cdot 4H_2O$ (0.20 mmol) and $Er(CH_3COO)_3 \cdot xH_2O$ (0.02 mmol) were mixed in a 100 mL three-neck round-bottom flask containing oleic acid (6 mL) and 1-octadecene (15 mL). The mixture was heated to 160℃ and stirred for 40 min. After stirring, the solution was cooled to room temperature. A methanol mixture, containing a solution of ammonium fluoride (4.0 mmol) and sodium hydroxide (2.5 mmol)

dissolved in methanol (5 mL) was added to the reaction flask and stirred for 40 minutes at 50℃. To remove the methanol, the reaction mixture was heated to 100℃ under vacuum with 15 minutes of stirring. Subsequently, the reaction flask was placed under a moderate flow of Argon and heated to 300℃ for 1 h. After cooling to room temperature again, ethanol was added to the reaction flask to precipitate the $NaYF_4$: Yb^{3+}, Er^{3+} nanoparticles. The precipitated UCNPs were isolated by centrifugation and washed several times with ethanol. The synthesized nanoparticles were redispersed in *n*-hexane.

The surface of the synthesized UCNPs were functionalized with PEG-Phospholipid according to a previously published method with minor modifications[4]. UCNPs dissolved in chloroform (2 mg/mL, 5 mL) were added to a mixture of mPEG (15 mg) and DSPE-PEG-NH_2 (5 mg) in chloroform (10 mL) and the reaction mixture was stirred for 30 minutes. After evaporating the solvent in the reaction mixture, the residue was incubated at 65℃ under a vacuum for 1 hour. To make a colorless and transparent suspension, 10 mL deionized water was added to the residue. The reaction mixture was filtered through a 0.45 μm cellulose acetate syringe filter. The amine-functionalized nanoparticles were washed twice with deionized water by centrifugation. The washed amine-functionalized UCNPs were then dispersed in 2 mL deionized water.

Characterization of UCNPs. The shape, uniformity, and size distribution of synthesized nanoparticles were determined by transmission electron microscope (TEM) (Tecnai G2 F30 S-Twin, Fei). The size of the synthesized UCNPs was about 24.2 ± 0.7 nm as shown in Figure S13. The ratio of lanthanide ions in the UCNPs was analyzed using inductively coupled plasma-mass spectroscopy (ICP-MS) (NexION 350D, Perkin-Elmer SCIEX). The ratio was Y: 78.573 %, Yb: 19.276 %, and Er: 2.151 % (Table S1). The crystal structure of UCNPs was assessed by the X-ray diffraction (XRD) pattern obtained from an X-ray diffractometer (SmartLab, RIGAKU). The XRD

pattern was consistent with the reported β type (hexagonal phase) UCNPs (Figure S14). The emission spectrum of the UCNPs was obtained using a spectrometer (QE 65000, Ocean Optics) with excitation with a 980 nm diode laser (1999CHP, 3SP Technologies) (Figure S15).

Cell culture and inhibition of dynein. SH-SY5Y neuroblastoma cells (Korea Cell Line Bank) were cultured in Dulbecco's Modified Eagle's Medium (DMEM, Hyclone) supplemented with 10 % fetal bovine serum (FBS, Hyclone), 100 units/mL penicillin, and 100 μg/mL streptomycin at 37℃ in a humidified 5 % CO_2 incubator. The cell suspension (1 mL at 1×10^4 cells/mL) was seeded onto a poly-D-lysine (Sigma-Aldrich) treated cover glass bottom dish (SPL) and incubated for 24 hours. For cell differentiation, 10 mM of retinoic acid (RA, Sigma-Aldrich) added to the cultured cells. Differentiation was allowed to proceed for more than ten days, and fresh culture medium containing 10 mM RA was added every two days. For dynein inhibition, cells were treated with 1 mM EHNA (Sigma-Aldrich) for 2 hours.

Wide-field Epi-Fluorescence Microscopy and Live Cell Imaging. The UCNPs in live neuroblastoma cells were imaged using an inverted microscope (IX73, Olympus). The wide-field epi-fluorescence microscope system (Figure S11) was comprised of EMCCD camera (iXON3, Andor Technology), a 980 nm diode laser (P161-600-980A, EM4 Inc.), and a live cell incubation chamber (TC-L-10, Live Cell Instrument). The incubation chamber controller maintained the temperature and CO_2 concentration at 37℃ and 5 % respectively during live cell imaging. For imaging, the dynein inhibited SH-SY5Y cells were washed three times with PBS (Gibco) and then treated with UCNPs for 30 min. Cells were washed three times using PBS to remove surplus UCNPs and phenol-red free DMEM medium was added to cover the glass bottom dish before imaging.

Image Processing. For z-sectioning of UCNPs, the piezo-electric stage was controlled using custom LabVIEW based sectioning software. The 2D section area and sectioning width were 102 μm × 37 μm (1024 pixels × 371 pixels with 0.101 μm/pixel) and 500 nm (covering range of z-axis) respectively. The scanning time (temporal resolution for SPT) was 100 ms (50 ms for each section image), which was set using built-in sectioning software. The two images obtained from one scan constituted one stack. The image acquisition process was carried out using Andor Solis software. The exposure time for EMCCD camera (iXON3, Andor Technology) was 50 ms. Figure S1 depicts the image sectioning and acquisition procedure through the z position *vs.* time (t_n). The trajectories of UCNPs were obtained from the series of image stacks using DiaTrack particle tracking software.

Data analysis. To explain the experimental data of the mean square displacement (MSD) and non-Gaussian parameter (NGP) using our models, we derived the analytic expressions of the second moment and the fourth moment of vesicle displacement along the microtubule for each model. Their explicit expressions are respectively given by

$$\langle d_x^2(t)\rangle = \langle R_x^2(t)\rangle + \langle x'^2\rangle, \quad \text{(M0-1)}$$

$$\langle d_x^4(t)\rangle = \langle R_x^4(t)\rangle + \langle x'^4\rangle + 6\langle R_x^2(t)\rangle\langle x'^2\rangle, \quad \text{(M0-2)}$$

where $\langle R_x^{2(4)}(t)\rangle$ denotes the second (fourth) moment of the MPM displacement distribution (See Method 2 for their explicit expressions in each model). $\langle x'^{2(4)}\rangle$ is the second (fourth) moment for the relative displacement of vesicles with respect to the MPM, whose values are respectively given by $1.26\times10^{-3}\,\mu m^2$ and $3.81\times10^{-6}\,\mu m^4$ (See Method 2, Section 2). Using the two moment expressions, we can calculate the NGP defined as $[\langle d_x^4(t)\rangle / 3\langle d_x^2(t)\rangle^2] - 1$. We optimize our models against the MSD and NGP data of vesicle displacement in the first 20 seconds, calculated from

119 vesicle transport trajectories. We also analyze the motion of vesicle in the microtubule-orthogonal direction; detailed methods are given in Method 2. (See also Figure S16).

To calculate the mean-first-passage time in Figure 3A, we perform accurate stochastic simulations for each of Model 1 and Model 2 with the optimized values of the adjustable parameters given in Table 1 or 2. The first passage times, at which a vesicle with the initial position identified as $x = 0$ reaches $x = -L$ or L for the first time, are collected from 10^4 simulation trajectories (See Method 3 for the detailed algorithms).

In Figure 3B, we compare the best-fitted result of eq 1 and experimental results of the mean-first-passage time. We obtain eq 1 for Model 1 by assuming that a mode-transition can occur only once. Each term on the right hand side of the equation can be calculated from

$$\tau_0(L) = \frac{L^2}{2D_0}\frac{\sinh\left(\sqrt{\zeta}\right)}{\sqrt{\zeta}\cosh^2\left(\sqrt{\zeta}\right)}\ , \qquad (\zeta = 2k_{1,0}L^2/D_0) \qquad \text{(M0-3)}$$

$$\tau_{0\to1}(L) = \left(\frac{L}{v} + \langle t_{0\to1}\rangle\right)\left(1-\operatorname{sech}\left(\sqrt{\zeta}\right)\right), \qquad \text{(M0-4)}$$

$$\tau_1(L) = \frac{L}{v}\exp\left(-k_{0,1}\frac{L}{v}\right), \qquad \text{(M0-5)}$$

$$\tau_{1\to0}(L) = \frac{L^2}{2D_0}\left[1-\left(\frac{v}{L}\right)^2\langle t_{1\to0}^2\rangle\right] + \langle t_{1\to0}\rangle, \qquad \text{(M0-6)}$$

where

$$\langle t_{0\to1}\rangle = \frac{1}{2k_{1,0}}\left(1-\frac{\sqrt{\zeta}\sinh\left(\sqrt{\zeta}\right)}{4\cosh\left(\sqrt{\zeta}\right)\sinh^2\left(\sqrt{\zeta}/2\right)}\right), \qquad (\zeta = 2k_{1,0}L^2/D_0) \qquad \text{(M0-7)}$$

$$\langle t_{1\to0}\rangle = \frac{1}{k_{0,1}}\left[1-(1+\xi)\exp(-\xi)\right], \qquad (\xi = k_{0,1}L/v) \qquad \text{(M0-8)}$$

$$\langle t_{1\to 0}^2 \rangle = \frac{2}{k_{0,1}^2}\left[1-\left(1+\xi+2^{-1}\xi^2\right)\exp\left(-\xi\right)\right]. \qquad \text{(M0-9)}$$

Here, D_0, v, and $k_{1,0}(k_{0,1})$ denote, respectively, the diffusion coefficient characterizing random motion of the MPM in the bidirectional mode, the speed of the MPM motion in the unidirectional mode, and the transition rate from the bidirectional (a unidirectional) mode to a unidirectional (the bidirectional) mode. A derivation of eq 1 is presented in Method 4.

Supplementary Method 2 | A detailed description of Model I and Model II

One can represent the cargo position vector $\mathbf{r}$ as $\mathbf{r}=\mathbf{R}+(\mathbf{r}-\mathbf{R})$, where $\mathbf{R}$ represents the position of the motor protein multiplex. $\mathbf{r}-\mathbf{R}$ designates the relative position of cargo with respect to the motor protein multiplex. Active motion of the motor protein multiplex affects the dynamics of $\mathbf{R}$, whereas passive thermal motion of cargo around the motor protein multiplex affects the dynamics of $\mathbf{r}-\mathbf{R}$. We assume the dynamics of $\mathbf{R}$ is not strongly correlated with the dynamics of $\mathbf{r}-\mathbf{R}$. In this section, we first present detailed descriptions of our model and the corresponding transport equations for both $\mathbf{R}$ and $\mathbf{r}-\mathbf{R}$. We then discuss how these two components comprise the dynamics of the cargo position, $\mathbf{r}$.

1. Dynamics of the motor protein multiplex

The motor protein multiplex (MPM) moves along the microtubule using chemical energy obtained from ATP-hydrolysis. Since catalytic activity of ATP-hydrolysis is dependent on the microscopic state of the motor protein multiplex, so too is the multiplex's transport dynamics. To provide a quantitative description of transport dynamics of the multi-mode MPM along the microtubule, let us first consider the following model for incremental motion of the MPM at mode Γ from position x to adjacent position $x+\Delta x$ along the microtubule: $\mathrm{MPM}(x,\Gamma)\rightleftarrows\mathrm{MPM}^*(x,\Gamma)\longrightarrow\mathrm{MPM}(x+\Delta x,\Gamma)$. Here, $\mathrm{MPM}(x,\Gamma)$ and $\mathrm{MPM}^*(x,\Gamma)$ designate, respectively, an MPM at mode Γ at position x along the microtubule and an activated MPM ready to perform mechanical motion by possibly multiple ATP-hydrolysis reactions of kinesins and dyneins in the MPM.

(a) ATP-hydrolysis dynamics

To describe the MPM mode-dependent dynamics of the ATP-hydrolysis coupled activation and subsequent mechanical motion along the microtubule, we extend the generalized enzyme

kinetics developed in refs.[5], as it provides a successful quantitative explanation of recent experimental data showing enzyme-state dependent catalytic activity[6]. In our model, each of the ATP-hydrolysis induced activation of MPM and the subsequent reactions of the activated MPM is modeled as Cox's renewal process[7], in which dynamics of an elementary reaction process is represented by the reaction time distribution. A schematic representation of this model is given by

$$\begin{aligned}
&\text{(a) } \mathrm{MPM}(x,\Gamma) \xrightarrow{\phi_{1,\Gamma}(t)} \mathrm{MPM}^*(x,\Gamma) \\
&\text{(b) } \mathrm{MPM}^*(x,\Gamma) \xrightarrow{\phi_{-1,\Gamma}(t)} \mathrm{MPM}(x,\Gamma) \qquad \text{(M0-10)} \\
&\text{(c) } \mathrm{MPM}^*(x,\Gamma) \xrightarrow{\phi_{2,\Gamma}(t)} \mathrm{MPM}(x+\Delta x,\Gamma)
\end{aligned}$$

In (M2-1), $\phi_1(t)$ denotes the reaction time distribution (RTD) of ATP-hydrolysis induced MPM activation; that is, $\phi_1(t)dt$ designates the probability that the MPM is activated and ready to move by ATP-hydrolysis reactions of motor proteins in time interval (*t*, *t* + *dt*), given that the MPM activation begins at time 0. $\phi_1(t)$ satisfies the following normalization condition, $\int_0^\infty dt\ \phi_1(t) = 1$. On the other hand, $\phi_{-1,\Gamma}(t)$ and $\phi_{2,\Gamma}(t)$ designate the RTDs of deactivation reaction (b) and mechanical motion to adjacent position (c) of the activated MPM at mode Γ, respectively. $\phi_{-1,\Gamma}(t)$ and $\phi_{2,\Gamma}(t)$ satisfy the following normalization conditions, $\int_0^\infty dt\ \phi_{-1,\Gamma}(t) = p_{-1,\Gamma}$ and $\int_0^\infty dt\ \phi_{2,\Gamma}(t) = p_{2,\Gamma}$ with $p_{-1,\Gamma} + p_{2,\Gamma} = 1$. Here, $p_{-1,\Gamma}$ or $p_{2,\Gamma}$ designates the probability of deactivation or mechanical motion of the activated MPM at mode Γ. If these reactions of the activated MPM are simple one-step Poisson processes, we have $\phi_{-1,\Gamma}(t) = k_{-1,\Gamma}\exp[-(k_{-1,\Gamma} + k_{2,\Gamma})t]$ and $\phi_{2,\Gamma}(t) = k_{2,\Gamma}\exp[-(k_{-1,\Gamma} + k_{2,\Gamma})t]$ where $k_{-1,\Gamma}$ and $k_{2,\Gamma}$ are the mode dependent rate constants. However, when the reactions of the activated MPM are multi-step processes, one can approximate

$\phi_{-1,\Gamma}(t)/p_{-1,\Gamma}$ or $\phi_{2,\Gamma}(t)/p_{2,\Gamma}$ by a gamma distribution, $\beta_\Gamma^{\alpha_\Gamma} t^{\alpha_\Gamma - 1} e^{-\beta_\Gamma t}/\Gamma(\alpha_\Gamma)$. For the sake of simplicity, we assume that $\phi_{-1,\Gamma}(t)/p_{-1,\Gamma}$ and $\phi_{2,\Gamma}(t)/p_{2,\Gamma}$ are the same, denoted by $\phi_{\mathrm{MPM}^*,\Gamma}(t)$.

For the scheme given in eq M0-10, we obtain the waiting time distribution, $\psi_\Gamma(t)$, or the distribution of time elapsed the MPM at mode Γ to move from one position to an adjacent position along the microtubule, as follows:

$$\hat{\psi}_\Gamma(s) = \frac{\hat{\phi}_1(s)\hat{\phi}_{2,\Gamma}(s)}{1-\hat{\phi}_{-1,\Gamma}(s)\hat{\phi}_1(s)} \tag{M0-11}$$

$\hat{\psi}_\Gamma(s)$ denotes the Laplace transform of $\psi_\Gamma(t)$, i.e., $\hat{\psi}_\Gamma(s) = \int_0^\infty dt e^{-st}\psi_\Gamma(t)$.

(b) ATP-hydrolysis-coupled transport dynamics

In this subsection, we present the transport equation of the MPM undergoing the ATP-hydrolysis-induced activation and subsequent incremental motion along the microtubule, as described by eq M2-1. Let us first consider a simple, hypothetical case where the MPM has only a single mode, $\Gamma_\pm$, at which the MPM moves in the $\pm$ direction on the microtubule. In this case, the probability, $p_m(t)$, that the multiplex is located at the *m*th site on the microtubule at time *t* satisfies the following equation [8]:

$$\hat{\dot{p}}_m(s) = \hat{\kappa}_{\Gamma_\pm}(s)\left[\hat{p}_{m\mp1}(s) - \hat{p}_m(s)\right] \tag{M0-12}$$

Here $\hat{\dot{p}}_m(s)$ and $\hat{p}_m(s)$ respectively designate the Laplace transforms of $\partial_t p_m(t)/\partial t$ and $p_m(t)$. In eq M0-12, $\hat{\kappa}_\Gamma(s)$ denotes the rate kernel given by

$$\hat{\kappa}_\Gamma(s) \equiv \frac{s\hat{\psi}_\Gamma(s)}{1-\hat{\psi}_\Gamma(s)} \tag{M0-13}$$

where $\hat{\psi}_\Gamma(s)$ is given by eq M0-11. Equation M0-12 describes unidirectional forward or backward motion of the motor protein multiplex with only a single conformational state.

By considering the continuum limit of eq M0-12, we obtain

$$\hat{\dot{p}}(x,s) = \mp \hat{K}_{\Gamma_\pm}(s)\frac{\partial \hat{p}(x,s)}{\partial x} \qquad \text{(M0-14)}$$

for the probability distribution, $p(x,t)$, of the multiplex's position, x, on the microtubule. With Δx being the distance between the adjacent sites on the microtubule, eq M0-14 can be easily derived from eq M0-12 by identifying $x = m\Delta x$, $\hat{p}_m(s) = \hat{p}(x,s)\Delta x$, and $\hat{p}_{m\mp1}(s) = \hat{p}(x \mp \Delta x, s)\Delta x$ and by using the Taylor series expansion, $\hat{p}(x \mp \Delta x, s) \cong \hat{p}(x,s) \mp \Delta x\left[\partial \hat{p}(x,s)/\partial x\right]$. In eq M0-14, $\hat{K}_{\Gamma_\pm}(s)$ denotes the drift kernel defined by

$$\hat{K}_{\Gamma_\pm}(s) \equiv \lim_{\Delta x \to 0} \hat{\kappa}_\Gamma(s)\Delta x \qquad \text{(M0-15)}$$

In Model 1 and Model 2, the motor protein multiplex not only exhibits unidirectional active motion but also exhibits bidirectional motion due to passive thermal motion or unbiased, seemingly random active motion when the multiplex is in the bidirectional mode in which the forward and backward forces by kinesins and dyneins in the MPM are in a delicate balance. The simplest extension of eq M0-14 to account for these bidirectional motions is given by

$$\hat{\dot{p}}(x,s) = \hat{D}_\Gamma(s)\frac{\partial^2 \hat{p}(x,s)}{\partial x^2} \mp \hat{K}_{\Gamma_\pm}(s)\frac{\partial \hat{p}(x,s)}{\partial x} \qquad \text{(M0-16)}$$

where $\hat{D}_\Gamma(s)\left\{\equiv (\Delta x_\Gamma^2/2)s\hat{\psi}_{x,\Gamma}(s)/\left[1-\hat{\psi}_{x,\Gamma}(s)\right]\right\}$ denotes the diffusion kernel describing the bidirectional motion of the motor protein multiplex along the microtubule. Δx_Γ and $\hat{\psi}_{x,\Gamma}(s)$ respectively represent the length scale and the waiting time distribution associated with the bidirectional motion along the microtubule of motor protein multiplex at state Γ. The explicit expression of $\hat{\psi}_{x,\Gamma}(s)$ conforms to eq M2-2.

When the time scale of the bidirectional motion is much shorter than the time scales of multiplex's unidirectional motion, $\hat{D}_\Gamma(s)$ can be approximated by the diffusion constant, $D_\Gamma\left(=\lim_{s\to 0}\hat{D}_\Gamma(s)\right)$. However, when the time scale of bidirectional motion is not separated from the time scales of the multiplex's unidirectional motion, this approximation cannot be used. For example, when $\psi_{x,\Gamma}(t)$ takes the following form:

$$\psi_{x,\Gamma}(t)=\frac{a_\Gamma}{b_\Gamma}\left(1+\frac{t}{b_\Gamma}\right)^{-(1+a_\Gamma)} \qquad (0<a_\Gamma<1) \tag{M0-17}$$

$\psi_{x,\Gamma}(t)$ has a heavy power-law tail, proportional to $t^{-(1+a_\Gamma)}$ $(0<a_\Gamma<1)$, and a finite time scale of thermal motion does not exist. It is known that, in this case, $\hat{D}_\Gamma(s)$ does not yield a finite diffusion constant in the small *s* limit, and thermal motion is described not by the simple diffusion operator but by the fractional diffusion operator. The Laplace transform of eq M0-17 is given by $\hat{\psi}_{x,\Gamma}(s)=a_\Gamma(sb_\Gamma)^{a_\Gamma}\exp(sb_\Gamma)\Gamma(-a_\Gamma,sb_\Gamma)$. Noting that $\hat{\psi}_{x,\Gamma}(s)$ can be expressed as $\hat{\psi}_{x,\Gamma}(s)\cong 1-(sb_\Gamma)^{a_\Gamma}\Gamma(1-a_\Gamma)$ in the small *s* limit and $\hat{\psi}_{x,\Gamma}(s)\cong(a_\Gamma/b_\Gamma)s^{-1}$ in the large *s* limit, we obtain the following asymptotic expressions for the diffusion kernel,

$$\hat{D}_\Gamma(s)\cong\begin{cases} D_{a_\Gamma}s^{1-a_\Gamma} & \text{as } s\to 0 \\ \dfrac{\Delta x_\Gamma^2 a_\Gamma}{2b_\Gamma}\left(=D_{a_\Gamma}\dfrac{a_\Gamma\Gamma(1-a_\Gamma)}{b_\Gamma^{1-a_\Gamma}}\right) & \text{as } s\to\infty \end{cases} \tag{M0-18}$$

where D_{a_Γ} is defined by $D_{a_\Gamma}=\Delta x_\Gamma^2/2b_\Gamma^{a_\Gamma}\Gamma(1-a_\Gamma)$.

In the special case where $\psi_\Gamma(t)$ and $\psi_{x,\Gamma}(t)$ can be approximated by exponential functions, $\hat{K}_{\Gamma_\pm}(s)$ and $\hat{D}_\Gamma(s)$ given in eqs M0-15 and M0-16 become constant, and eq M0-16 reduces to the well-known Fokker-Planck equation describing Brownian motion under a constant force field[9].

We can further extend eq M0-16 to describe the transport dynamics of the multi-state motor protein multiplex that undergoes mode-transitions as follows:

$$\hat{\dot{p}}(x,\Gamma,s) = \hat{D}_{\Gamma}(s)\frac{\partial^2 \hat{p}(x,\Gamma,s)}{\partial x^2} - \hat{K}_{\Gamma}(s)\frac{\partial \hat{p}(x,\Gamma,s)}{\partial x} + L(\Gamma)\hat{p}(x,\Gamma,s) \qquad \text{(M0-19)}$$

Here $\hat{p}(x,\Gamma,s)$ denotes the Laplace transform of the joint probability density, $p(x,\Gamma,t)$, of the motor protein multiplex at mode Γ at position, x, along the microtubule at time t. In eq M0-19, $L(\Gamma)$ denotes a mathematical operator describing the mode-transition dynamics of theMPM. Equation M0-19 takes a simpler form in the Fourier domain, i.e.,

$$\tilde{\hat{\dot{p}}}(\omega,\Gamma,s) = -\omega^2 \hat{D}_{\Gamma}(s)\tilde{\hat{p}}(\omega,\Gamma,s) - i\omega\hat{K}_{\Gamma}(s)\tilde{\hat{p}}(\omega,\Gamma,s) + L(\Gamma)\tilde{\hat{p}}(\omega,\Gamma,s) \qquad \text{(M0-20)}$$

where $\tilde{\hat{p}}(\omega,\Gamma,s)$ denotes the Fourier transform of $\hat{p}(x,\Gamma,s)$, defined by $\tilde{\hat{p}}(\omega,\Gamma,s) \equiv \int_{-\infty}^{\infty} dx \exp(-i\omega x)\hat{p}(x,\Gamma,s)$. Equation M0-19 or M0-20 is the general form of the transport equation applicable to any specific model for conformation-dependent transport of the motor protein multiplex on the microtubule.

In the present work, we employ motor protein multiplex models with multiple distinct modes, $\{\Gamma_i\}$. For such models, eq M0-20 becomes

$$\begin{aligned}\tilde{\hat{\dot{p}}}(\omega,\Gamma_i,s) = &-\omega^2 \hat{D}_i(s)\tilde{\hat{p}}(\omega,\Gamma_i,s) - i\omega\hat{K}_i(s)\tilde{\hat{p}}(\omega,\Gamma_i,s) \\ &+ \sum_j \left[k_{i,j}\tilde{\hat{p}}(\omega,\Gamma_j,s) - k_{j,i}\tilde{\hat{p}}(\omega,\Gamma_i,s) \right]\end{aligned} \qquad \text{(M0-21)}$$

for each $\tilde{\hat{p}}(\omega,\Gamma_i,s)$. In eq M0-21, $\hat{D}_i(s)$ and $\hat{K}_i(s)$ denote $\hat{D}_i(s) \equiv \hat{D}_{\Gamma_i}(s)$ and $\hat{K}_i(s) \equiv \hat{K}_{\Gamma_i}(s)$, respectively. $k_{j,i}$ denotes the transition rate from mode Γ_i to mode Γ_j. Equation M0-21 for all states can be collectively written as

$$\tilde{\hat{\dot{\mathbf{P}}}}(\omega,s) = \left[-\omega^2 \hat{\mathbf{D}}(s) - i\omega\hat{\mathbf{K}}(s) + \mathbf{L} \right] \cdot \tilde{\hat{\mathbf{P}}}(\omega,s) \qquad \text{(M0-22)}$$

where $\tilde{\tilde{\mathbf{P}}}(\omega, s)$ denotes the column vector, the *i*th element of which is given by $\tilde{\tilde{p}}(\omega, \Gamma_i, s)$. In eq M0-22, the *ij*th elements of $\hat{\mathbf{D}}(s)$, $\hat{\mathbf{K}}(s)$, and $\mathbf{L}$ are respectively given by

$$\left(\hat{\mathbf{D}}(s)\right)_{ij} = \hat{D}_i(s)\delta_{ij} \tag{M0-23}$$

$$\left(\hat{\mathbf{K}}(s)\right)_{ij} = \hat{K}_i(s)\delta_{ij} \tag{M0-24}$$

and

$$(\mathbf{L})_{ij} = -\delta_{ij}\sum_n k_{n,j} + (1-\delta_{ij})k_{i,j} \tag{M0-25}$$

In eq M0-24, the analytic expression of $\hat{K}_i(s)$ is given by

$$\hat{K}_i(s) = \Delta x \frac{p_{2,i} s\hat{\phi}_{1,i}(s)\hat{\phi}_{\mathrm{MPM}^*,\mathrm{i}}(s)}{1-\hat{\phi}_{1,i}(s)\hat{\phi}_{\mathrm{MPM}^*,\mathrm{i}}(s)} \tag{M0-26}$$

where $\hat{\phi}_{\mathrm{MPM}^*,\mathrm{i}}(s)$ are related to $\hat{\phi}_{-1,\Gamma}(s)$ and $\hat{\phi}_{2,\Gamma}(s)$ in eq M0-11 by $\hat{\phi}_{\mathrm{MPM}^*,\mathrm{i}}(s) = \hat{\phi}_{-1,\Gamma_i}(s)\big/ p_{-1,\Gamma_i} = \hat{\phi}_{2,\Gamma_i}(s)\big/ p_{2,\Gamma_i}$. $\phi_{\mathrm{MPM}^*,\mathrm{i}}(t)$ is nothing but the lifetime distribution of the activated MPM at mode Γ_i. Equation M2-17 can be obtained by substituting eq M0-11 into eq M0-13 and eq M0-15. In eq M0-26, $\hat{\phi}_{1,i}(s)\hat{\phi}_{\mathrm{MPM}^*,\mathrm{i}}(s)$ denotes the Laplace-transformed RTD of the two successive processes: the ATP hydrolysis induced MPM activation and the subsequent deactivation or mechanical motion of the activated MPM at mode Γ_i. We have analyzed our experimental data by assuming that $\phi_{\mathrm{MPM}^*,\mathrm{i}}(t)$ is a gamma distribution ($\equiv \beta_i^{\alpha_i} t^{\alpha_i - 1} e^{-\beta_i t}\big/\Gamma(\alpha_i)$), because it can represent a multi-step process ranging from a sub-Poisson to super-Poisson process. For this model, $\hat{\phi}_{\mathrm{MPM}^*,\mathrm{i}}(s)$ is given by $\left[\beta_i\big/(s+\beta_i)\right]^{\alpha_i}$ where α_i and β_i are defined as $\alpha_i = \langle t_{\mathrm{MPM}^*,i}\rangle^2 \big/ \langle \delta t^2_{\mathrm{MPM}^*,i}\rangle$ and $\beta_i = \langle t_{\mathrm{MPM}^*,i}\rangle \big/ \langle \delta t^2_{\mathrm{MPM}^*,i}\rangle$, with $t_{\mathrm{MPM}^*,i}$ being the stochastic lifetime of

the activated MPM at mode Γ_i. In addition, $\hat{\phi}_{1,i}(s)$ is assumed to be $\hat{\phi}_{1,i}(s) = (1+s/k_1([\mathrm{ATP}]))^{-1}$ with $k_1([\mathrm{ATP}])$ being the rate of the ATP hydrolysis-induced MPM activation. The corresponding drift kernel and the waiting time distribution of the MPM at state Γ_i are respectively given by

$$\hat{K}_i(s) = \Delta x \frac{p_{2,i} s}{\left[1+s/k_{1,i}([\mathrm{ATP}])\right](1+s/\beta_i)^{\alpha_i} - 1} \cong v_i \frac{(\alpha_i/\beta_i)\, s}{(1+s/\beta_i)^{\alpha_i} - 1} \qquad \text{(M0-27a)}$$

$$\hat{\psi}_i(s) = \frac{p_{2,i}}{\left[1+s/k_{1,i}([\mathrm{ATP}])\right](1+s/\beta_i)^{\alpha_i} - 1 + p_{2,i}} \qquad \text{(M0-27b)}$$

In eq M2-18a, $v_i\left[\equiv \hat{K}_i(0)\right]$ denotes the mean velocity of ballistic motion of the MPM at unidirectional mode Γ_i. v_i can be expressed as

$$v_i = \Delta x\left(p_{2,i}/\left\langle t_{\mathrm{MPM*,i}}\right\rangle\right)\left[1+\left(k_{1,i}([\mathrm{ATP}])\left\langle t_{\mathrm{MPM*,i}}\right\rangle\right)^{-1}\right]^{-1} \qquad \text{(M2-18c)}$$

In the special case where $k_{1,i}([\mathrm{ATP}])$ is linear in the ATP concentration, eq M2-18 reduces to the Michaelis-Menten equation[10]. In eq M0-27a, the second equality effectively holds on the basis of the assumption that ATP hydrolysis-induced MPM activation occurs much faster than subsequent reactions of the activated MPM. This assumption is valid at a typical value of cytosolic ATP concentration, e.g., [ATP] = 1 mM[11].

Noting that $\tilde{\dot{\mathbf{P}}}(\omega,s) = s\tilde{\tilde{\mathbf{P}}}(\omega,s) - \tilde{\mathbf{P}}(\omega,0)$, one can obtain the solution of eq M0-22 as

$$\tilde{\tilde{\mathbf{P}}}(\omega,s) = \left[\left(s\mathbf{I} + \omega^2\hat{\mathbf{D}}(s)\right) + i\omega\,\hat{\mathbf{K}}(s) - \mathbf{L}\right]^{-1} \cdot \tilde{\mathbf{P}}(\omega,0) \qquad \text{(M0-28)}$$

If we choose the initial position, x_0, of the motor protein multiplex to be the origin of the x coordinate, the initial value of $p(x,\Gamma_i,t=0)$ is given by $p_i^{ss}\delta(x)$ with p_i^{ss} being the probability of mode Γ_i in the steady-state. For the initial condition, $\tilde{\mathbf{P}}(\omega,0)$ in eq M0-28 is given by

$\left[\tilde{\mathbf{P}}(\omega,0)\right]_j = p_j^{ss}$. With this initial condition at hand, one can obtain the analytic expression for each component of $\tilde{\hat{\mathbf{P}}}(\omega,s)$ from eq M0-28. The Fourier-Laplace transform of the probability density function of the position of the motor protein multiplex on the microtubule is given by the sum of all the elements of $\tilde{\hat{\mathbf{P}}}(\omega,s)$, i.e.

$$\tilde{\hat{P}}(\omega,s) = \sum_j \tilde{\hat{p}}(\omega,\Gamma_j,s) \qquad \text{(M0-29)}$$

From eq M0-29, we can calculate the time-dependent distribution, $P(x,t)$, of the MPM's position along the microtubule and its various moments.

The general solution given in eq M0-28 is applicable to various special models including Model 1 and Model 2, which are discussed in the following sections (c) and (d).

(c) Model 1

In this subsection, we discuss Model 1 shown in Figure 2A. For Model 1, we employ a motor protein multiplex model with three distinct conformation states, $\{\Gamma_{-1},\Gamma_0,\Gamma_{+1}\}$. A motor protein multiplex has one bidirectional state, Γ_0, and two unidirectional states, $\Gamma_{\pm 1}$, one for anterograde and the other for retrograde direction. For this model, we have $\hat{K}_0(s)=0$. On the other hand, the multiplex at state $\Gamma_{\pm 1}$ undergoes unidirectional motion with the state-dependent drift kernel, $\hat{K}_{\pm 1}(s)$.

Our experimental data show that the velocity and displacement distributions of the motor protein multiplexes are bilaterally symmetric. To construct a model consistent with the experimental data, we assume $\hat{K}_{-1}(s) = -\hat{K}_{+1}(s)$ and that the following pairs of state transitions occur with the same rate:

(a) $0 \xrightarrow{k_{+1,0}} +1$ and $0 \xrightarrow{k_{-1,0}} -1$

(b) $+1 \xrightarrow{k_{0,+1}} 0$ and $-1 \xrightarrow{k_{0,-1}} 0$ (M0-30)

According to eq M0-30, we have $k_{+1,0} = k_{-1,0} = k_{1,0}$, $k_{0,+1} = k_{0,-1} = k_{0,1}$.

The vector, $\tilde{\hat{\mathbf{P}}}(\omega, s)$, and the matrices, $\hat{\mathbf{D}}(s)$, $\hat{\mathbf{K}}(s)$, and $\mathbf{L}$ in eq M0-28 are then given by

$$\tilde{\hat{\mathbf{P}}}(\omega, s) \equiv \begin{pmatrix} \tilde{\hat{p}}(\omega, \Gamma_{+1}, s) \\ \tilde{\hat{p}}(\omega, \Gamma_{0}, s) \\ \tilde{\hat{p}}(\omega, \Gamma_{-1}, s) \end{pmatrix} \quad \text{(M0-31)}$$

$$\mathbf{D}_{3\times 3} = \begin{pmatrix} 0 & 0 & 0 \\ 0 & D_0 & 0 \\ 0 & 0 & 0 \end{pmatrix} \quad \text{(M0-32)}$$

$$\hat{\mathbf{K}}_{3\times 3}(s) = \begin{pmatrix} \hat{K}_1(s) & 0 & 0 \\ 0 & 0 & 0 \\ 0 & 0 & -\hat{K}_1(s) \end{pmatrix}, \quad \text{(M0-33)}$$

and

$$\mathbf{L}_{3\times 3} = \begin{pmatrix} -k_{0,1} & k_{1,0} & 0 \\ k_{0,1} & -2k_{1,0} & k_{0,1} \\ 0 & k_{1,0} & -k_{0,1} \end{pmatrix}. \quad \text{(M0-34)}$$

The simplest mathematical description of the bidirectional motion of the multiplex at state Γ_0 is to employ diffusion operator, $D_0 \, \partial^2 \hat{p}(x, \Gamma_0, s) / \partial x^2$. For state Γ_0, $\hat{D}_0(s)$ appearing in eq M0-23 is set equal to constant $D_0 \left[= \lim_{s \to 0} \hat{D}_0(s) \right]$ in eq M0-32. For the other states, the bidirectional motion of the multiplex is not considered in Model 1.

The *s*-dependent drift kernel, $\hat{K}_i(s)$, eventually becomes constant in the small-*s* limit, as far as the mean time, $\langle t_i \rangle$, for $\hat{\psi}_i(s)$ exists. In other words, $\hat{K}_i(s)$ can be treated as its small-*s* limit

value, i.e., $\hat{K}_i(s=0)=v_i$, when displacement data at times much longer than $\langle t_i \rangle$ are analyzed. (see Figure S17).

(d) Model 2

In this subsection, we discuss Model 2 shown in Figure 2A. For Model 2, we employ a motor protein multiplex model with five distinct conformation states, $\{\Gamma_{-2},\Gamma_{-1},\Gamma_0,\Gamma_{+1},\Gamma_{+2}\}$. A motor protein multiplex has one bidirectional state, Γ_0, and four unidirectional states, $\Gamma_{\pm1}$ and $\Gamma_{\pm2}$, two for anterograde and the others for retrograde direction. For this model, we have $\hat{K}_0(s)=0$. On the other hand, the multiplex at states $\Gamma_{\pm1}$ and $\Gamma_{\pm2}$ undergoes unidirectional motion with state-dependent drift kernels, $\hat{K}_{\pm1}(s)$ and $\hat{K}_{\pm2}(s)$.

Our experimental data show that the velocity and displacement distributions of the motor protein multiplexes are bilaterally symmetric. To construct a model consistent with the experimental data, we assume $\hat{D}_{-1}(s)=\hat{D}_{+1}(s)$ and $\hat{D}_{-2}(s)=\hat{D}_{+2}(s)$, $\hat{K}_{-1}(s)=-\hat{K}_{+1}(s)$ and $\hat{K}_{-2}(s)=-\hat{K}_{+2}(s)$, and that the following pairs of state transitions occur with the same rate:

$$
\begin{aligned}
&\text{(a) } 0 \xrightarrow{k_{+1,0}} +1 \text{ and } 0 \xrightarrow{k_{-1,0}} -1\\
&\text{(b) } +1 \xrightarrow{k_{0,+1}} 0 \text{ and } -1 \xrightarrow{k_{0,-1}} 0\\
&\text{(c) } +1 \xrightarrow{k_{+2,+1}} +2 \text{ and } -1 \xrightarrow{k_{-2,-1}} -2\\
&\text{(d) } +2 \xrightarrow{k_{+1,+2}} +1 \text{ and } -2 \xrightarrow{k_{-1,-2}} -1\\
&\text{(e) } +2 \xrightarrow{k_{0,+2}} 0 \text{ and } -2 \xrightarrow{k_{0,-2}} 0\\
&\text{(f) } 0 \xrightarrow{k_{+2,0}} +2 \text{ and } 0 \xrightarrow{k_{-2,0}} -2
\end{aligned}
\qquad \text{(M0-35)}
$$

According to eq M0-35, we have $k_{+1,0}=k_{-1,0}=k_{1,0}$, $k_{0,+1}=k_{0,-1}=k_{0,1}$, $k_{+2,+1}=k_{-2,-1}=k_{2,1}$, $k_{+1,+2}=k_{-1,-2}=k_{1,2}$, $k_{0,+2}=k_{0,-2}=k_{0,2}$, and $k_{+2,0}=k_{-2,0}=k_{2,0}$.

The vector, $\tilde{\hat{\mathbf{P}}}(\omega,s)$, and the matrices, $\hat{\mathbf{D}}(s)$, $\hat{\mathbf{K}}(s)$, and $\mathbf{L}$ in eq M0-28 are then given by

$$\tilde{\tilde{\mathbf{P}}}(\omega,s)\equiv\begin{pmatrix}\tilde{\tilde{p}}(\omega,\Gamma_{+2},s)\\ \tilde{\tilde{p}}(\omega,\Gamma_{+1},s)\\ \tilde{\tilde{p}}(\omega,\Gamma_{0},s)\\ \tilde{\tilde{p}}(\omega,\Gamma_{-1},s)\\ \tilde{\tilde{p}}(\omega,\Gamma_{-2},s)\end{pmatrix} \tag{M0-36}$$

$$\hat{\mathbf{D}}(s)=\begin{pmatrix}\hat{D}_2(s) & 0 & 0 & 0 & 0\\ 0 & \hat{D}_1(s) & 0 & 0 & 0\\ 0 & 0 & \hat{D}_0(s) & 0 & 0\\ 0 & 0 & 0 & \hat{D}_1(s) & 0\\ 0 & 0 & 0 & 0 & \hat{D}_2(s)\end{pmatrix} \tag{M0-37}$$

$$\hat{\mathbf{K}}(s)=\begin{pmatrix}\hat{K}_2(s) & 0 & 0 & 0 & 0\\ 0 & \hat{K}_1(s) & 0 & 0 & 0\\ 0 & 0 & 0 & 0 & 0\\ 0 & 0 & 0 & -\hat{K}_1(s) & 0\\ 0 & 0 & 0 & 0 & -\hat{K}_2(s)\end{pmatrix} \tag{M0-38}$$

and

$$\mathbf{L}=\begin{pmatrix}-k_{1,2}-k_{0,2} & k_{2,1} & k_{2,0} & 0 & 0\\ k_{1,2} & -k_{2,1}-k_{0,1} & k_{1,0} & 0 & 0\\ k_{0,2} & k_{0,1} & -2k_{1,0}-2k_{2,0} & k_{0,1} & k_{0,2}\\ 0 & 0 & k_{1,0} & -k_{2,1}-k_{0,1} & k_{1,2}\\ 0 & 0 & k_{2,0} & k_{2,1} & -k_{1,2}-k_{0,2}\end{pmatrix} \tag{M0-39}$$

Unlike Model 1, a more general, alternative description of the bidirectional motion of the multiplex at state Γ_0 can be made by employing the generalized diffusion operator, $\hat{D}_0(s)\partial^2\hat{p}(x,\Gamma_0,s)/\partial x^2$. Here, $\hat{D}_0(s)$ is given by

$$\hat{D}_0(s)\cong D_{a_0}\left[s^{a_0-1}+\frac{{b_0}^{1-a_0}}{a_0\Gamma(1-a_0)}\right]^{-1}, \tag{M0-40a}$$

which is an approximate diffusion kernel interpolating between the two limit expressions in eq M0-18 for state Γ_0. In eq M0-40, a_0 and b_0 denotes $a_0 \equiv a_{\Gamma_0}$ and $b_0 \equiv b_{\Gamma_0}$, respectively. The bidirectional motion at the other states, $\Gamma_{i\neq 0}$, originates from passive thermal motion alone. We model passive thermal motion of the MPM in unidirectional modes by fractional diffusion, that is described by

$$\hat{D}_i(s) = D_i s^{a_i - 1} \quad \text{(i=1, 2).} \qquad \text{(M2-31b)}$$

We find that Model 2 provides a better quantitative explanation of experimental results than its alternative with thermal motion of the MPM being assumed to be simple diffusion.

As shown in Figure 2, both Model 1 and Model 2 can explain the experimental data of the MSD and the NGP. However, as we can see in Figure 2E to H, Model 1 is in good agreement with the experimental result at times longer than 10 seconds. On the other hand, Model 2 provides a quantitative prediction of the cargo displacement distribution at all times between 0.1 second and 20 seconds.

(e) Other multi-state models

The significance of the bidirectional active motion at state Γ_0 can be evaluated by using Model 1′ and Model 2′, where the multiplex at state Γ_0 undergoes no bidirectional, unbiased motion, according to which eqs M0-32 and M0-37 are respectively replaced by

$$\mathbf{D}_{3\times 3} = \begin{pmatrix} 0 & 0 & 0 \\ 0 & 0 & 0 \\ 0 & 0 & 0 \end{pmatrix} \tag{M0-41}$$

and

$$\hat{\mathbf{D}}(s) = \begin{pmatrix} \hat{D}_2(s) & 0 & 0 & 0 & 0 \\ 0 & \hat{D}_1(s) & 0 & 0 & 0 \\ 0 & 0 & 0 & 0 & 0 \\ 0 & 0 & 0 & \hat{D}_1(s) & 0 \\ 0 & 0 & 0 & 0 & \hat{D}_2(s) \end{pmatrix} \tag{M0-42}$$

On the other hand, the motion of the multiplex at unidirectional states for each model is modeled to be the same as in its original version.

As shown in Figure S8, Model 1′ and Model 2′ can also explain the experimental data of the MSD and the NGP. However, both models fail to explain the cargo displacement distribution, especially the central portion of the distribution at intermediate-to-long times, implying that the bidirectional active motion at state Γ_0 is important in order to explain the experimental data as shown in Figure S8.

2. Dynamics of relative motion of cargo with respect to the motor protein multiplex

In our experiment, we observe the vesicle carried by the motor protein multiplex, not the motor protein multiplex. The stochastic dynamics of the vesicle position results not only from transport of the motor protein multiplex on the microtubule, but also from relative thermal motion of the cargo with respect to the multiplex. In this subsection, we describe our model for the relative thermal motion of the cargo with respect to the motor protein multiplex.

The relative motion of cargo can be directly monitored by inhibiting dynein motor proteins with EHNA, which effectively localizes the entire motor protein multiplex. From the experimental data, we find that cargo undergo stochastic motion, but the variance of the cargo position hardly increases with time when the motor protein multiplex is localized. We model the relative motion of cargo with respect to the motor protein multiplex as thermal motion in a potential well.

The potential field imposed on the cargo can be heterogeneous depending on the conformation of the motor protein complex. For a given configuration of the motor protein multiplex, we model the relative motion of the cargo as an Ornstein-Uhlenbeck (OU) process, the simplest stochastic process occurring in a harmonic potential. The curvature of the potential imposed on the cargo position is dependent on the configuration of the motor protein complex.

For this model, the probability density, $f(x',t)$, of the cargo's relative position with respect to the motor protein multiplex at a given conformation is described by the Fokker-Planck equation of the OU process,

$$\frac{\partial}{\partial t} f\left(x',t\right) = D\frac{\partial}{\partial x'}\left[\frac{\partial}{\partial x'} + \kappa x'\right] f\left(x',t\right) \qquad \text{(M0-43)}$$

where D and κ denote, respectively, the diffusion coefficient of cargo and the force constant associated with a harmonic potential scaled by thermal energy, which is dependent on the motor protein conformation. The solution to eq M0-43 is known to be

$$f\left(x',t\,|\,x_0',0\right)=\left(\frac{\kappa}{2\pi\left(1-e^{-2D\kappa t}\right)}\right)^{1/2}\exp\left(-\frac{\kappa}{2}\frac{\left(x'-x_0'e^{-D\kappa t}\right)^2}{1-e^{-2D\kappa t}}\right) \qquad \text{(M0-44)}$$

where $f\left(x',t\,|\,x_0',0\right)$ denotes the probability density of the cargo's position under the initial condition that the cargo is located at x_0' at time 0. At long times, eq M2-35 approaches the equilibrium distribution.

Our experimental data shows that the relative separation between the cargo and the motor protein multiplex quickly relaxes to the equilibrium distribution; the variance in the relative separation is found to be nearly constant throughout measurement times ranging from 0.1 second to 2.0 seconds. Therefore, we assume the equilibrium distribution for the relative separation between cargo and the multiplex:

$$f\left(x'\right)\cong\left(\frac{\kappa}{2\pi}\right)^{1/2}\exp\left(-\frac{\kappa}{2}x'^2\right). \qquad \text{(M0-45)}$$

The stationary distribution given in eq M0-45 is Gaussian but, as shown in Figure S4B, the experimentally measured distribution of the cargo position has a non-Gaussian, exponential tail. To explain the experimental data, we assume that the force constant, κ, scaled by thermal energy is distributed depending on the MPM conformation. The experimentally measured stationary distribution of the cargo position is quantitatively explainable by assuming that κ is a random variable given by $\kappa=\kappa_0/(1+q^2)$ with κ_0 and q being a constant and Gaussian random variable, respectively. For this model, the steady-state distribution of cargo position, x, is given by

$$f\left(x'\right)=\int_{-\infty}^{\infty}dq\sqrt{\frac{\kappa_0}{2\pi\left(1+q^2\right)}}\exp\left(-\frac{\kappa_0 x'^2}{2\left(1+q^2\right)}\right)N(q\,|\,\sigma_q^2) \qquad \text{(M0-46)}$$

where $N(q\,|\,\sigma_q^2)$ denotes $\left(2\pi\sigma_q^2\right)^{-1/2}\exp\left[-q^2/(2\sigma_q^2)\right]$. This result is used to explain the experimental data shown in Figure 2D. The optimized values of the adjustable parameters are as follows: $\kappa_0^{-1}=1.99\times10^{-4}\,\mu\text{m}^2$ and $\sigma_q^2=5.30$. The variance $\langle x'^2\rangle$ of $f(x)$ is given by

$$\langle x'^2\rangle=\kappa_0^{-1}(1+\sigma_q^2)\cong1.25\times10^{-3}\mu\text{m}^2. \qquad \text{(M0-47)}$$

Thus far we have discussed the distribution of the relative position of cargo with respect to the motor protein multiplex in the microtubule direction. We find that eq M0-46 can explain the distribution of the cargo position in the microtubule-orthogonal direction as well, not only when the motor protein multiplex is inhibited, but also when the motor protein multiplex is not inhibited. However, when the motor protein multiplex is in motion, the variance of the cargo position in the microtubule-orthogonal direction slightly increases with time. We ascribe this phenomenon to rare transitions of the motor protein multiplex from one microtubule to another (see Section 3.2 below).

3. Dynamics of cargo carried by the motor protein multiplex

3.1 Cargo motion in the microtubule direction

Cargo motion along the microtubule is contributed from both ATP-hydrolysis coupled motion of the motor protein complex, described in Section 1, and passive thermal motion of cargo, described in Section 2. In this section, we discuss how these two different types of motion compose cargo motion in the microtubule direction, or the direction of the x axis.

The cargo position, x, can be represented by $x=R_x+(x-R_x)$ where R_x represents a given position of the motor protein complex. The distribution of R_x is designated by $P(R_x,t)$, whose Fourier-Laplace transform is given in eq M0-28, and the distribution of $x-R_x\,(\equiv x')$ is $f(x')$ given in eq M0-46. The probability distribution, $g(x,t)$, of the cargo position, *x*, is then given by

$$g(x,t) = \int_{-\infty}^{\infty} dR_x \int_{-\infty}^{\infty} dx' \delta(x - R_x - x') P(R_x, t) f(x') \\ = \int_{-\infty}^{\infty} dx' P(x - x', t) f(x') \tag{M0-48}$$

which is correct as long as passive thermal motion of cargo is independent of the ATP-hydrolysis coupled motion of the motor protein complex. By taking the Fourier transform on both sides of eq M0-48, we obtain

$$\tilde{g}(\omega, t) = \tilde{P}(\omega, t) \tilde{f}(\omega) \tag{M0-49a}$$

or

$$\tilde{\tilde{g}}(\omega, s) = \tilde{\tilde{P}}(\omega, s) \tilde{f}(\omega) \tag{M0-49b}$$

where $\tilde{\tilde{P}}(\omega, s)$ and $\tilde{f}(\omega) \left[= \int_{-\infty}^{\infty} dx' \exp(-i\omega x') f(x') \right]$ are given by eq M0-29 and

$$\tilde{f}(\omega) = \frac{\exp\left(-\frac{\omega^2}{2\kappa_0} \right)}{\sqrt{\frac{\omega^2}{\kappa_0} \sigma_q^2 + 1}} \tag{M0-50}$$

respectively.

We can easily obtain the *n*th moment, $\langle d_x^n(t) \rangle \left(\equiv \int_{-\infty}^{\infty} x^n g(x,t) dx \right)$, of the cargo distribution by using the following relationship, $\langle d_x^n(t) \rangle = (i^n) \lim_{\omega \to 0} \partial^n \tilde{g}(\omega, t) / \partial \omega^n$. The first and all other odd moments vanish because the cargo distribution is a symmetric function of x . The second moment, $\langle d_x^2 \rangle$, of the cargo distribution, $g(x,t)$, is given by

$$\langle d_x^2(t) \rangle = \langle R_x^2(t) \rangle + \langle x'^2 \rangle \tag{M0-51}$$

where $\langle R_x^2(t) \rangle$ and $\langle x'^2 \rangle$ denote the second moments of $P(R_x, t)$ and $f(x')$, respectively. Here, $\langle R_x^2(t) \rangle$ can be calculated by taking the inverse Laplace transform of $-\lim_{\omega \to 0} \partial^2 \tilde{\tilde{P}}(\omega, s) / \partial \omega^2$

with $\tilde{\tilde{P}}(\omega,s)$ given in eq M0-28. $\langle x'^2\rangle$ is a constant in time and given by $\langle x'^2\rangle = \kappa_0^{-1}\left(1+\sigma_q^2\right)$ (see eq M0-47). The mean square displacement (MSD) of cargo displacement can be directly calculated from eq M0-51. At short times where the MPM has yet to undergo a mode transition, a simple analytic expression of the vesicle MSD is obtained

$$\langle d_x^2(t)\rangle \cong 2p_0D_0t + (1-p_0)v_\pm^2t^2 + \langle x'^2\rangle \qquad \text{(Model 1)} \qquad \text{(M0-52a)}$$

$$\langle d_x^2(t)\rangle \cong 2p_0D_0\frac{a_0\Gamma(1-a_0)}{b_0^{1-a_0}}t + (2p_{\pm1}v_{\pm1}^2 + 2p_{\pm2}v_{\pm2}^2)t^2 + \langle x'^2\rangle \qquad \text{(Model 2)} \qquad \text{(M0-52b)}$$

where $\langle x'^2\rangle$ denotes the contribution to the MSD from the fast thermal motion of vesicle with respect to the MPM (see eq M0-47).

The fourth moment of the cargo distribution, $g(x,t)$, is given by

$$\langle d_x^4(t)\rangle = \langle R_x^4(t)\rangle + \langle x'^4\rangle + 6\langle R_x^2(t)\rangle\langle x'^2\rangle \qquad \text{(M0-53)}$$

where $\langle R_x^4(t)\rangle$ and $\langle x'^4\rangle$ are given by the inverse Laplace transform of $\lim_{\omega\to0}\partial^4\tilde{\tilde{P}}(\omega,s)/\partial\omega^4$ with $\tilde{\tilde{P}}(\omega,s)$ given in eq M0-28 and $3\kappa_0^{-2}\left(1+2\sigma_q^2+3\sigma_q^4\right)$, respectively.

The non-Gaussian parameter (NGP), $\alpha_{2,x}(t)$, which measures deviation of the distribution of cargo displacement from Gaussian, can be calculated from eqs M0-51 and M0-53 by the following equation:

$$\begin{aligned}\alpha_{2,x}(t) &\equiv \frac{\langle d_x^4(t)\rangle}{3\langle d_x^2(t)\rangle^2} - 1 \\ &= \frac{\langle R_x^2(t)\rangle^2}{\langle d_x^2(t)\rangle^2}\alpha_2\left(R_x,t\right) + \frac{\langle x'^2\rangle^2}{\langle d_x^2(t)\rangle^2}\alpha_2\left(x',t\right)\end{aligned} \qquad \text{(M0-54)}$$

$\alpha_2(x',t)$ is constant in time and given by $2\sigma_q^4/\left(1+\sigma_q^2\right)^2$. With $\alpha_2(R_x,t)\left[\equiv\langle R_x^4(t)\rangle/\left(3\langle R_x^2(t)\rangle^2\right)-1\right]$ calculated from $\langle R_x^4(t)\rangle = \lim_{\omega\to0}\partial^4\tilde{\tilde{P}}(\omega,s)/\partial\omega^4$ and

$\langle R_x^2(t)\rangle = -\lim_{\omega\to 0}\partial^2\tilde{\tilde{P}}(\omega,s)\big/\partial\omega^2$, eq M0-53, $\alpha_{2,x}(t)$ calculated from eq M0-53 provides an excellent quantitative explanation of the experimental results for the time dependence of the NGP. The optimized values of the adjustable parameters are given in Tables 1 and 2.

3.2 Cargo motion in the microtubule-orthogonal direction

The cargo position, *y*, in the microtubule-orthogonal direction can also be represented by $y = R_y + (y - R_y)$, where R_y represents the position of the motor protein multiplex in the microtubule-orthogonal direction. As the motor protein multiplex usually moves in the microtubule direction, the position of the motor protein multiplex in the microtubule-orthogonal direction does not change significantly at short times. At short times, the cargo dynamics in the microtubule-orthogonal direction is mostly contributed from the dynamics of $y - R_y (\equiv y')$, the relative position of cargo with respect to the motor protein complex. We find that, at short times, the cargo displacement distribution, $h(y,t)$, in the microtubule-orthogonal direction is in good agreement with $f(x)$ defined in eq M0-46, the cargo displacement distribution when the motor multiplex is immobilized by EHNA. That is, $h(y,t) \cong f(y)$ (at short times). This result indicates that thermal random motion of cargo relative to the motor protein multiplex is not greatly influenced by EHNA dynein inhibition.

At times longer than 1.0 second, cargo displacement exhibits sub-diffusive dynamics and its MSD slowly increases with time, being proportional to $t^{0.7}$. The magnitude of the MSD in the microtubule-orthogonal direction is negligible compared with the MSD along the microtubule. We ascribe anomalous transport in the microtubule-orthogonal direction to the motor protein complex's motion from one microtubule to another. The simplest model that describes this type of transition is the continuous time random walk (CTRW) model. Adopting this model, we assume

that a motor protein complex's transition from one microtubule to another is Cox's renewal process, which is characterized by a single sojourn time distribution, $\psi_y(t)$. The corresponding hydrodynamic limit transport equation describing the displacement distribution, $Q(y,t)$, of the motor protein multiplex is given by

$$\hat{\dot{Q}}(y,s) = \hat{D}_y(s)\,\partial^2 \hat{Q}(y,s)/\partial y^2 \tag{M0-55}$$

where $\hat{D}_y(s) = \left(\Delta y^2/2\right) s\,\hat{\psi}_y(s)\Big/\left[1-\hat{\psi}_y(s)\right]$ with Δy being the mean distance between adjacent microtubules. In eq M0-55 $\hat{\dot{Q}}(y,s)$ and $\hat{Q}(y,s)$ denote Laplace transforms of $\partial Q(y,t)/\partial t$ and $Q(y,t)$, respectively. The solution of eq M0-55 under the initial condition, $Q(y,0)=\delta(y)$, can be obtained as

$$\hat{Q}(y,s) = \frac{1}{\sqrt{4s\hat{D}_y(s)}} \exp\left[-\sqrt{\frac{y^2 s}{\pi \hat{D}_y(s)}}\right] \tag{M0-56}$$

Using a derivation similar to the derivation of eq M0-49, we can obtain the cargo displacement distribution in the microtubule-orthogonal direction as

$$h(y,t) = \int_{-\infty}^{\infty} dy' Q(y-y') f(y') \tag{M0-57}$$

$$\tilde{h}(\omega,t) = \tilde{Q}(\omega,t)\,\tilde{f}(\omega) \tag{M0-58a}$$

$$\tilde{\hat{h}}(\omega,s) = \tilde{\hat{Q}}(\omega,s)\,\tilde{f}(\omega) \tag{M0-58b}$$

where $\tilde{\hat{Q}}(\omega,s)$ and $f(\omega)$ are given by $\tilde{\hat{Q}}(\omega,s) = \left[s+\omega^2 \hat{D}_y(s)\right]^{-1}$ and eq M0-50, respectively. Noting that eq M0-58 has the same mathematical structure as eq M0-49, we can obtain the analytic expression for the second and fourth moments, and the NGP for the microtubule in the same manner that we obtain eqs M0-51 ~ M0-54 from eq M0-49. The MSD in the microtubule-

orthogonal direction or the second moment of the displacement distribution, $h(y,t)$, is obtained as

$$\langle d_y^2(t)\rangle = 2\hat{L}^{-1}\left[\hat{D}_y(s)/s^2\right] + \langle y'^2\rangle \qquad \text{(M0-59)}$$

Here $\hat{L}^{-1}$ denotes the inverse Laplace transform operator. Because cargo displacement resulting from passive thermal motion is nearly isotropic (Figure 2D), we set the value of $\langle y'^2\rangle$ to be the same as $\langle x'^2\rangle$, i.e., $\langle y'^2\rangle = \langle x'^2\rangle = 1.26\times10^{-3}\,\mu\text{m}^2$. It is well known that the long-time power-law dependence of the MSD can be explained by the CTRW when $\psi_y(t)$ has a heavy power-law tail, proportional to $t^{-(1+a)}$ $(0<a<1)$. In the present work, we choose the following form for $\psi_y(t)$:

$$\psi_y(t) = \frac{a}{b}\left(1+\frac{t}{b}\right)^{-(1+a)} \qquad (0<a<1). \qquad \text{(M0-60)}$$

The Laplace transform of eq M0-60 is given by $\hat{\psi}_y(s) = a(sb)^a \exp(sb)\Gamma(-a, sb)$. Noting that the small *s* expansion of $\hat{\psi}_y(s)$ is given by $\hat{\psi}_y(s) \cong 1-(sb)^a\Gamma(1-a)$, one obtains

$$\hat{D}_y(s)\left\{\equiv(\Delta y^2/2)s\hat{\psi}_y(s)/\left[1-\hat{\psi}_y(s)\right]\right\} \cong D_y^a s^{1-a} \qquad \text{(M0-61)}$$

D_y^a defined as $\Delta y^2/2b^a\Gamma(1-a)$. Substituting eq M0-61 into eq M0-59, we obtain

$$\langle d_y^2(t)\rangle \cong \frac{\Delta y^2}{\Gamma(1-a)\Gamma(1+a)}(t/b)^a + \langle y'^2\rangle \qquad \text{(M0-62)}$$

Equation M0-62 provides a quantitative explanation of the experimental results for the MSD (Figure S6). The optimized values of the adjustable parameters are given in Table S2.

Supplementary Method 3 | Simulation method for mean-first-passage time

In this method, we present a detailed simulation algorithm used to calculate the mean-first-passage times of our models in Figure 3. Here, fast thermal motion of the vesicle relative to the motor protein multiplex is not explicitly taken into account because such a motion is localized to very small region around the multiplex.

At the very beginning of a vesicle trace, a vesicle's initial state is determined with the steady-state probability, eq N1-3, of each state, whose numerical values are calculated with the optimized values of the rate parameters given in Tables 1 and 2. The vesicle's initial position, $x(t=0)$, is always set to be zero. When a vesicle stays at state *j*, the associated duration time is given by the smallest time, $t_{i^*,j}$, among times, $\{t_{i,j}\}$, sampled from $k_{ij}e^{-tk_{ij}}$ for each state *i* linked to state *j*. Here, $t_{i,j}$ designates the duration time at state *j* until the transition from state *j* to state *i* occurs. When the simulation time elapses by $t_{i^*,j}$, the state of the vesicle is changed from state *j* to state *i**. During which the vesicle stays at state *j* for $t_{i^*,j}$, the vesicle's position, *x*, along the microtubule axis is updated every time step, $\Delta t(=10^{-5}$ seconds$)$, and the update algorithm depends on the model we simulate. For Model 1, the update equation is given by

$$x(t+\Delta t) = x(t) + v_1\Delta t(1-\delta_{0j}) + \sqrt{2D_0\Delta t}N(0,1)\delta_{0j} \qquad \text{(M0-63)}$$

where $N(0,1)$ denotes the Gaussian random number with zero mean and unit variance. For Model 2, we need to simulate a subdiffusive motion characterized by the state-dependent diffusion kernel, $\hat{D}_j(s)$. When *j* = ±1 or ±2, $\hat{D}_j(s)$ is given by $\hat{D}_j(s) = D_{a_j}s^{1-a_j}$. In this case, the simulation method developed on the basis of the subordination approach[12, 13] can be used:

$$u(\tau+\Delta\tau)=u(\tau)+\Delta\tau^{1/a_j}\xi,$$
$$x(\tau+\Delta\tau)=x(\tau)+(2D_{a_j}\Delta\tau)^{1/2}N(0,1) \qquad \text{(M0-64)}$$

where ξ is the totally skewed positive α-stable random number generated by

$$\xi=\frac{\sin[a_j(V+\pi/2)]}{(\cos V)^{1/a_j}}\left(\frac{\cos[V-a_j(V+\pi/2)]}{W}\right)^{\frac{1-a_j}{a_j}} \qquad \text{(M0-65)}$$

In eq M0-65, V is the uniform random number distributed over $(-\pi/2,\pi/2)$, and W is the random number sampled from an exponential distribution with unit mean. $x(\tau)$ and $u(\tau)$ are simultaneously updated every internal time step, $\Delta\tau(=10^{-8}\ \mathrm{s}^{a_j})$, until $u(\tau+\Delta\tau)$ is greater than $t+\Delta t$. Once the condition required to stop updating x and u is satisfied, $x(\tau+\Delta\tau)$ is identified as $x(t+\Delta t)$. Then, we add the constant drift contribution, $v_j\Delta t$, to $x(t+\Delta t)$.

On the other hand, to our best knowledge, there does not exist any available simulation algorithm for subdiffusion with $\hat{D}_0(s)=D_{a_0}\left[s^{a_0-1}+b_0^{1-a_0}/a_0\Gamma(1-a_0)\right]^{-1}$ given in eq M0-40. On the basis of the fact that $\hat{D}_0(s)$ approaches $D_{a_0}s^{1-a_0}$ in the small-s limit, and $\hat{D}_0(\infty)=D_{a_0}\,a_0\Gamma(1-a_0)/b_0^{1-a_0}$ in the large-s limit, we here adopt an approximate method in which eqs M0-64 and M0-65 with $a_j=a_0$ and $D_{a_j}=D_{a_0}$ are used when $t_{i^*,j}\le 1/s_c\ (\cong 24\ \text{seconds})$, where s_c is the intersection point between $D_{a_0}s^{1-a_0}$ and $\hat{D}_0(\infty)$, i.e., $D_{a_0}s_c^{1-a_0}=\hat{D}_0(\infty)$, and the Brownian dynamics simulation with the diffusion coefficient, $\hat{D}_0(\infty)$, is performed otherwise. In the latter case, the update equation is given by

$$x(t+\Delta t)=x(t)+\sqrt{2\hat{D}_0(\infty)\Delta t}\,N(0,1) \qquad \text{(M0-66)}$$

To calculate the mean-first-passage time, we generate 10^4 vesicle traces that last up to the time when $x(t)$ reaches $L_{\max}$ or $-L_{\max}$ for the first time, where $L_{\max}$ is the maximum length we consider. From such traces, we can easily calculate the mean-first-passage time for any L shorter than $L_{\max}$. A first passage time is here defined as the time when $x(t)$ reaches L or $-L$ for the first time in a single trace. The mean-first-passage times of Model 1 and Model 2 for a given L are presented in Figure 3A of the main text.

Supplementary Method 4 | Derivation of eq 1

Here, we present a derivation of eq 1. The first two terms on the R.H.S. of eq 1 take into account the contribution of the initial bidirectional mode to the MFPT, while the last two terms account for the contribution of the initial ballistic mode to the MFPT. Equation 1 is only an approximate result, which is obtained by assuming that mode-transition of the MPM can take place only once. However, the result of eq 1 is in qualitative agreement with exact simulation results of Model 1 and experimental data for the MFPT (see Figure 3B).

1. Derivation of $\tau_0(L)$ and $\tau_1(L)$ in eq 1

$\tau_i(L)$ denotes the average of the first passage time of the MPM without any mode-transition. In terms of mathematics, $\tau_i(L)$ is given by $\tau_i(L) = \int_0^\infty dt\, f_i(L,t)\exp(-t/t_i)t$ where $f_i(L,t)\exp(-t/t_i)$ designates the distribution of time at which the motor protein multiplex in mode *i* first passes travel length L, given that the MPM does not undergo a mode-transition as of the first passage time. Here t_i denotes the lifetime of the MPM in mode *i*.

$f_0(L,t)$ can be obtained by using the known relation between the first passage time and the survival probability, $f_0(L,t) = -\partial_t S_0(t,L)$, where survival probability $S_0(t,L)$ can be calculated from $S_0(t,L) = \int_{-L}^{L} dx p_0(x,t)$, where $p_0(x,t)$ is a probability distribution of the MPM displacement. $p_0(x,t)$ satisfies the diffusion equation, $\partial_t p_0(x,t) = D\partial_x^2 p_0(x,t)$, under the absorbing boundary condition, $p_0(\pm L,t) = 0$, and the following initial condition, $p_0(x,0) = \delta(x)$, where $\delta(x)$ denotes Dirac's delta function. $f_1(L,t)$ is simply given by $\delta(t - L/v)$. The resulting analytic expressions of $\tau_0(L)$ and $\tau_1(L)$ are presented in eqs M0-3 and M0-5 in Method 1.

2. Derivation of $\tau_{0\to1}(L)$

$\tau_{0\to1}(L)$ in eq 1 represents the MFPT of the MPMs over travel length *L* given that each MPM undergoes mode-transition $0\to1$ as of the first passage time. Analytic expressions of $\tau_{0\to1}(L)$ can be obtained by noting that the sum of the travel length x_0 of the MPM in mode 0 and travel length x_1 mode 1 must be the same as the total travel length L, i.e., $x_0(t_{0\to1})+x_1(t_{FPT}-t_{0\to1})=L$, where $t_{0\to1}$ being the time at which the mode transition takes place. From this equation and $x_1(t)=vt$, we obtain $t_{FPT}=\left[L-x_0(t_{0\to1})\right]/v+t_{0\to1}$. Noting that the mean of $x_0(t_{0\to1})$ is zero for a symmetric diffusion process and the distribution of $t_{0\to1}$ is given by $2k_{1,0}\exp(-2k_{1,0}t)S_0(L,t)$, we obtain eq M0-4 for $\tau_{0\to1}(L)$.

3. Derivation of $\tau_{1\to0}(L)$

$\tau_{1\to0}(L)$ in eq 1 represents the MFPT of the MPMs over travel length *L* given that each MPM undergoes mode-transition $1\to0$ as of the first passage time. Let us consider an MPM that undergoes mode-transition $1\to0$ at time $t_{0\to1}$ before the first passage of travel length *L*. Right after mode-transition time $t_{1\to0}$, the motor protein multiplex is located at $x_0(t_{1\to0})=\pm vt_{1\to0}$ in mode 0. Noting that the MFPT of the MPM in mode 0, initially located at x_0, is given by $\left(L^2/2D_0\right)\left[1-\left(x_0/L\right)^2\right]$, we obtain the MFPT of the MPM that undergoes mode-transition $1\to0$ at time $t_{1\to0}$ by $\left(L^2/2D_0\right)\left[1-(vt_{1\to0})^2/L^2\right]+t_{1\to0}$. $\tau_{1\to0}(L)$ given in eq M0-6 can be obtained by taking average of this result over the distribution of the mode-transition time, $t_{1\to0}$, which is given by $k_{0,1}\exp(-k_{1,0})\Theta(L-vt)$ with $\Theta(x)$ being Heaviside step function.

4. Derivation of eq 1

Noting that $\tau_0(L)+\tau_{0\to1}(L)$ are the MFPT of the MPM initially prepared at mode 0 and $\tau_1(L)+\tau_{1\to0}(L)$ are the MFPT of the MPM initially prepared at mode 1, we can obtain the MFPT of the MPM with initial probabilities of 0 and ±1 modes being p_0 and $p_{\pm1}$ as $p_0\left[\tau_0(L)+\tau_{0\to1}(L)\right]$ $+\left(p_{+1}+p_{-1}\right)\left[\tau_1(L)+\tau_{1\to0}(L)\right]$. Noting that $p_{+1}+p_{-1}=1-p_0$, we obtain eq 1. p_0 is related to $k_{1,0}$ and $k_{0,1}$ by $p_0=k_{0,1}/(k_{0,1}+2k_{1,0})$.

5. Asymptotic behavior of the MFPT

At short travel lengths over which the vesicle's first passage occurs much faster than mode-transition, the eq 1 reduces to

$$\overline{\tau}_{FPT}(L)\cong p_0 L^2/2D_0+(1-p_0)L/v, \qquad (L<\sqrt{D/(2k_{1,0})},\ v/k_{0,1}) \tag{M0-67}$$

Equation M0-67 becomes exact in the slow state-transition limit. The MFPT in eq M0-67 obeys diffusive scaling, $L^2/2D$, in the bidirectional mode only limit ($p_0=1$), but ballistic scaling, L/v in the unidirectional mode only limit. In our system, the value of p_0 is given by 0.979 and the MFPT has mostly ballistic scaling over short travel lengths (Figure 3A and 3B).

Under the bidirectional mode-dominant initial condition, the scaling behavior of the MFPT switches from the diffusive scaling to ballistic scaling at $L>\sqrt{D/2k_{1,0}}$ when the MPM undergoes a transition from the initial bidirectional mode to a unidirectional mode. In the ballistic scaling regime, eq 1 is approximately given by

$$\overline{\tau}_{FPT}(L)\cong p_0\overline{\tau}_{0\to1}(L)+(1-p_0)\overline{\tau}_1(L) \quad (\sqrt{D/2k_{1,0}}<L<v/k_{0,1}) \tag{M0-68}$$

At travel lengths far longer than $\sqrt{D/2k_{1,0}}$ and $v/k_{0,1}$, the MFPT given in eq 1 recovers diffusive scaling

$$\bar{\tau}_{FPT}(L) \approx L^2/(2D_\infty) \qquad (\sqrt{D/2k_{1,0}},\ v/k_{0,1} << L) \qquad \text{(M0-69)}$$

where D_∞ denotes the terminal diffusion coefficient of the MPM. Because eq 1 is only an approximate result, it does not yield a correct expression of D_∞. However, it is possible to calculate the exact analytic expression of D_∞, which is given by eq N1-3a for Model 1. For Model 2 as well, the MFPT obeys eq M0-69 with D_∞ given in eq N1-3b in at long travel lengths.

Supplementary Note 1 | The analytical expression of the long-time diffusion coefficient for Model 1 and Model 2.

For Model 1 and Model 2, the long-time diffusion coefficient, D_∞ , defined by $D_\infty = \lim_{t\to\infty} \langle d_x^2(t)\rangle / 2t$, can be calculated as

$$D_\infty = D_0 p_0 + \int_0^\infty dt \langle v_t v_{t=0}\rangle \qquad \text{(Model 1)} \qquad \text{(N1-1a)}$$

$$D_\infty = \int_0^\infty dt \langle v_t v_{t=0}\rangle \qquad \text{(Model 2)} \qquad \text{(N1-1b)}$$

on the basis of the Green-Kubo relation [14]. For Model 1, the bidirectional diffusive motion at state 0 contributes to the long-time limit behavior of the mean-square displacement, while for Model 2, the bidirectional subdiffusive motion at state 0 does not. $\langle v_t v_{t=0}\rangle$ denotes the time correlation function of mode-dependent velocity fluctuation, explicitly,

$$\langle v_t v_{t=0}\rangle = (v_1, 0, -v_1)\cdot e^{t\mathbf{L}}\cdot (v_1 p_{+1}, 0, -v_1 p_{-1})^T \qquad \text{(Model 1)} \qquad \text{(N1-2a)}$$

$$\langle v_t v_{t=0}\rangle = (v_2, v_1, 0, -v_1, v_2)\cdot e^{t\mathbf{L}}\cdot (v_2 p_{+2}, v_1 p_{+1}, 0, -v_1 p_{-1}, v_2 p_{-2})^T \qquad \text{(Model 2)} \qquad \text{(N1-2b)}$$

where the superscript *T* stands for the transpose of a row vector. In eqs N1-2a and N1-2b, the state-to-state transition matrix, **L**, is given by eq M0-34 for Model 1 and eq M0-39 for Model 2. $p_i [= \lim_{t\to\infty} (e^{t\mathbf{L}})_{ij}]$ denotes the steady-state probability of state *i* and satisfies the even symmetry with respect to the interchange between state *i* and state –*i*, i.e., $p_i = p_{-i}$, because of the bilateral symmetry conditions, eq M0-30 for Model 1 and eq M0-35 for Model 2. For both models, the explicit expressions of p_i 's are given by

$$\begin{cases} p_0 = \dfrac{k_{0,1}}{k_{0,1} + 2k_{1,0}} \\ p_1 = \dfrac{k_{1,0}}{k_{0,1} + 2k_{1,0}} \end{cases} \qquad \text{(Model 1)} \qquad \text{(N1-3a)}$$

$$\begin{cases} p_0 = \dfrac{k_{0,1}k_{0,2} + k_{0,1}k_{1,2} + k_{0,2}k_{2,1}}{k_{0,1}k_{0,2} + k_{0,1}k_{1,2} + k_{0,2}k_{2,1} + 2(k_{1,0}k_{1,2} + k_{1,0}k_{0,2} + k_{1,2}k_{2,0}) + 2(k_{2,0}k_{2,1} + k_{2,0}k_{0,1} + k_{2,1}k_{1,0})} \\ p_1 = \dfrac{k_{1,0}k_{1,2} + k_{1,0}k_{0,2} + k_{1,2}k_{2,0}}{k_{0,1}k_{0,2} + k_{0,1}k_{1,2} + k_{0,2}k_{2,1} + 2(k_{1,0}k_{1,2} + k_{1,0}k_{0,2} + k_{1,2}k_{2,0}) + 2(k_{2,0}k_{2,1} + k_{2,0}k_{0,1} + k_{2,1}k_{1,0})} \\ p_2 = \dfrac{k_{2,0}k_{2,1} + k_{2,0}k_{0,1} + k_{2,1}k_{1,0}}{k_{0,1}k_{0,2} + k_{0,1}k_{1,2} + k_{0,2}k_{2,1} + 2(k_{1,0}k_{1,2} + k_{1,0}k_{0,2} + k_{1,2}k_{2,0}) + 2(k_{2,0}k_{2,1} + k_{2,0}k_{0,1} + k_{2,1}k_{1,0})} \end{cases}$$

(Model2) (N1-3b)

Substituting eqs N1-2 and N1-3 into eq N1-1 for each model, we have

$$D_\infty = D_0 p_0 + (1 - p_0) v_1^2 / k_{0,1} \quad \text{(Model 1)} \quad \text{(N1-4a)}$$

$$D_\infty = 2\frac{(k_{0,2} + k_{1,2})v_1^2 p_1 + (k_{2,1}p_1 + k_{1,2}p_2)v_1 v_2 + (k_{0,1} + k_{2,1})v_2^2 p_2}{k_{0,1}k_{0,2} + k_{0,1}k_{1,2} + k_{0,2}k_{2,1}} \quad \text{(Model 2)} \quad \text{(N1-4b)}$$

Supplementary Note 2 | Effects of vesicle delivery by inhibition of cytoplasmic dynein

In this note, we briefly discuss of the effects of vesicle delivery by inhibition of cytoplasmic dynein. EHNA, which selectively inhibits ATP-hydrolysis of dyneins, strongly suppresses vesicle-delivery by the MPM within our measurement time (Figure. 1, C and D). Upon dynein inhibition by EHNA, the VDD shows negligible change over time and is nearly isotropic (Figure. S18, A to D); both the MSD and the NGP have the same order of magnitudes in all directions and exhibit no significant time dependence (Figure S18, E and F). This means that dynein inhibition by EHNA results in MPM localization on the microtubule. Upon EHNA-induced MPM localization, the VDD has nearly the same shape as the VDD free of dynein inhibition at 0.1 seconds. This observation is consistent with the assumption about the isotropic VDD at short times which originates from fast thermal motion of the vesicle bound to the MPM, not from the MPM's active motion.

Supplementary Note 3 | Motor protein multiplex displacement distribution

For both Model 1 and Model 2, we obtain analytic expressions of the MPM displacement distribution in the Fourier-Laplace domain (Method 2, Section 1). For an accurate quantitative explanation of vesicle transport dynamics, it is necessary to account for thermal motion of the vesicle bound to the MPM. The distribution of distance between the vesicle and the MPM is directly obtainable from the VDD for the case when the MPM is stalled on the microtubule by EHNA-induced dynein inhibition (Figure 2D). The experimentally measured distribution of the distance between the vesicle and the MPM is found to be stationary in our experimental time scale and is well-represented by a superposition of Gaussian with the variance being a statically distributed random variable (Method 2, Section 2). The displacement distribution of the vesicle bound to the MPM is given by the convolution of the MPM displacement distribution and the distribution of distance between cargo and the multiplex. From the analytic expression of the vesicle displacement distribution, we can easily obtain the analytic results of the MSD and NGP for both Model 1 and Model 2 in the Laplace domain.

For Model 2, the mean speed of unidirectional motion is estimated to be 0.182 μm/s for the MPM in the slow-moving mode (± 1) and 1.28 μm/s in the fast-moving mode (2.50×10^{-3} $\mu m^2/s$). In addition to this unidirectional motion, the MPM undergoes random motion resulting from random fluctuating force exerted by various molecules in the cell environment. When we assume random motion of the MPM along the microtubule is sub-diffusive motion, the prediction of Model 2 in good agreement with experimental results for the VDD at all times investigated (Figure 2, E to H). The sub-diffusive random motion is modeled by fractional diffusion. The transitions between the multiplex states are found to be far slower than individual ATP-hydrolysis coupled motion and occur in a wide range of time scales (Tables 1 and 2).

SUPPLEMENTARY FIGURES

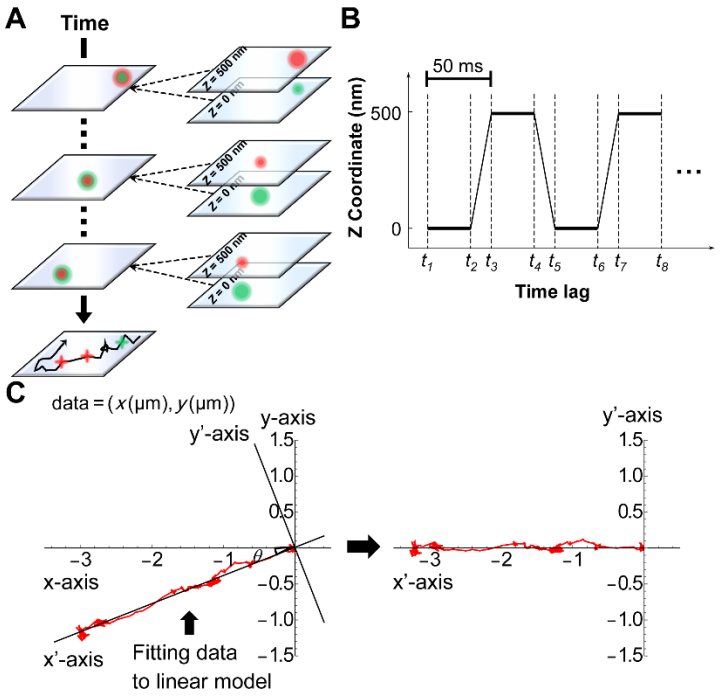

Figure S1. Schematic illustration of single particle tracking (SPT) of UCNPs in living cells. (A) Scheme of double-plane imaging based 2D SPT using wide-field epi-fluorescence microscopy. The piezo objective scanner covered 500 nm along the z-axis. This technique allows for a far longer measurement time than single focus imaging techniques. (B) Z-axis scanning time-profile. A series of image stacks was obtained by continuous z-axis scanning with the piezo objective scanner. The exposure time (the interval between $t_i \sim t_{i+2}$) to obtain one image was 50 ms. (C) The microtubule direction is identified as the most probable direction of cargo motion. For each trajectory, the coordinates of the cargo position are transformed so that the x-axis in the new coordinate lies in the microtubule direction.

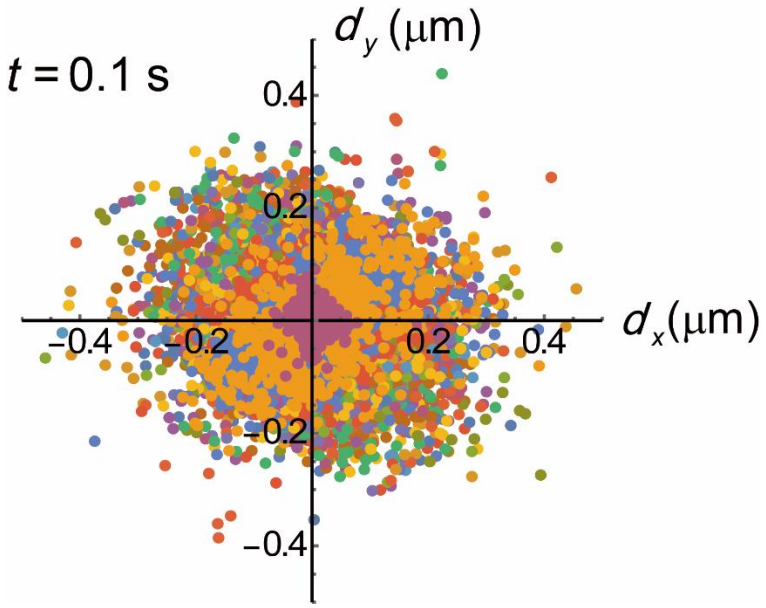

Figure S2. Two-dimensional representation of the displacement trajectories along axonal microtubule when measurement time bin is 0.1 second for uninhibited cells. The vesical displacement distribution is nearly isotropic when the measurement time is 0.1 seconds.

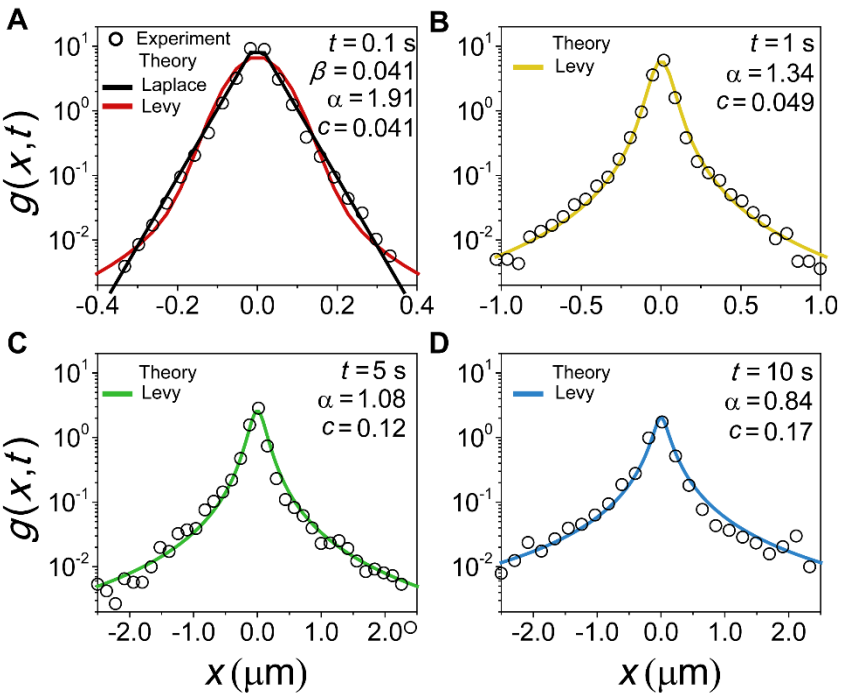

Figure S3. Probability distribution, $g(x,t)$, of cargo displacement in the microtubule direction fitted by Lévy alpha-stable distribution. Probability distribution of cargo displacement in the microtubule direction has a shape similar to a Laplace distribution proportional to $e^{-\beta|x|}$ at 0.1 second and a Lévy alpha-stable distribution with a tail distribution given by $c^{\alpha}\sin(\pi\alpha/2)(\Gamma(\alpha+1)/\pi)/|x|^{1+\alpha}$ at times longer than roughly 0.4 s. The optimized value of c and α are dependent on the measurement time as shown in the figures. (circles) Experimental data, (black line) best fitted result of the Laplace distribution with the optimized value of β at 0.1 second, (colored line) best fitted result of the Lévy distribution at four different measurement times.

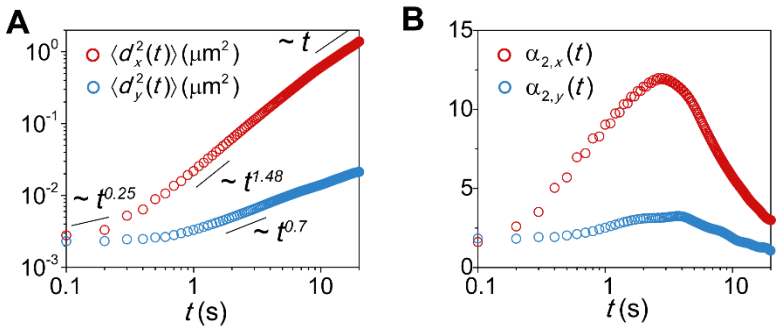

Figure S4. The Mean square displacement and non-Gaussian parameter of cargo displacement. (red circles) experimental data in the microtubule direction, (blue circles) experimental data in microtubule-orthogonal direction. Cargo motion in the microtubule-orthogonal direction shows a slow, sub-diffusive dynamics and super-Gaussian process.

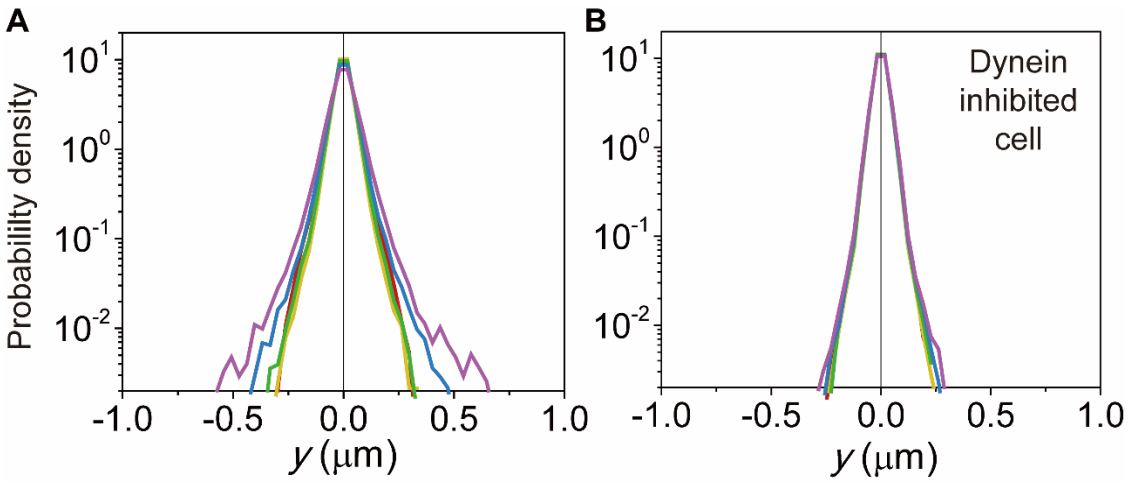

Figure S5. The distribution of the cargo displacement in the microtubule-orthogonal direction. The distribution of (A) Normal cell and (B) dynein inhibited cell shows nearly same structure and time-independent shape.

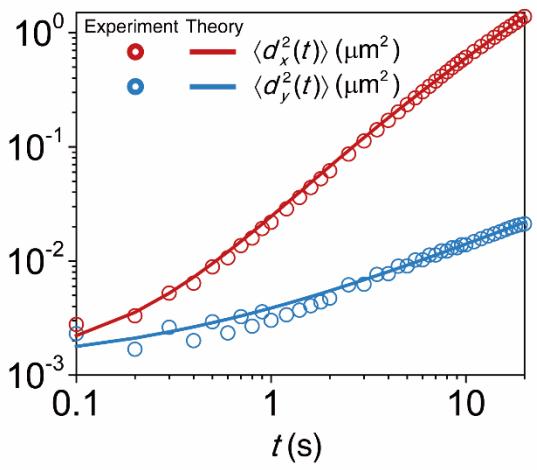

Figure S6. Mean square displacement of cargo motion in the microtubule direction and in the microtubule-orthogonal direction. (red circles) Experimental data for the MSD in the microtubule direction, (red line) result of our model shown in Figure 2A from the main text [eq M0-49]. (blue circles) experimental data for the MSD in the microtubule-orthogonal direction, (blue line) result of our model described in Method 2 [eq M0-62]. Note that the MSD in the microtubule-orthogonal direction is negligible compared with the MSD in the microtubule direction.

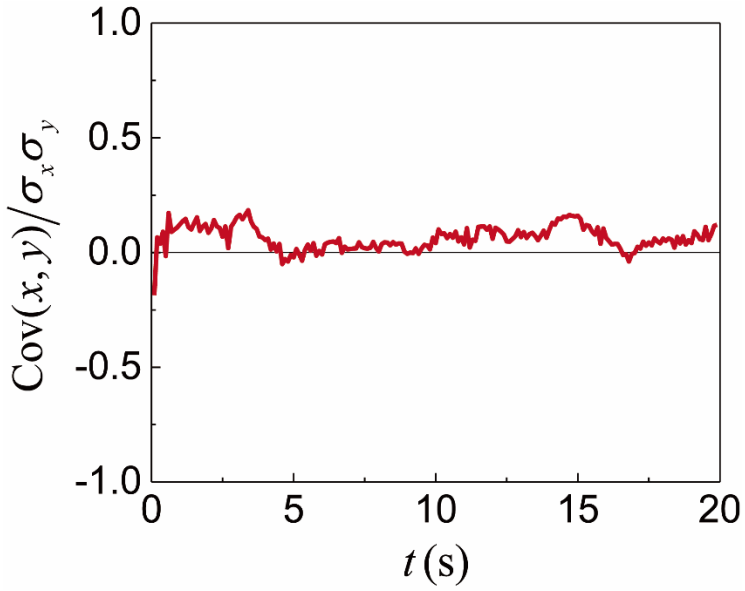

Figure S7. Correlation between cargo motion in microtubule direction and in the microtubule-orthogonal direction. In this figure, $\mathrm{Cov}(x, y)$ denotes the covariance of *x* and *y*, and σ_x, σ_y denote the standard deviation of *x* and *y*. The Pearson correlation coefficient, $\mathrm{Cov}(x, y)/\sigma_x\sigma_y$, has nearly zero value with small fluctuation with respect to time, which means the little correlation of motion of cargo between the microtubule and microtubule-orthogonal direction.

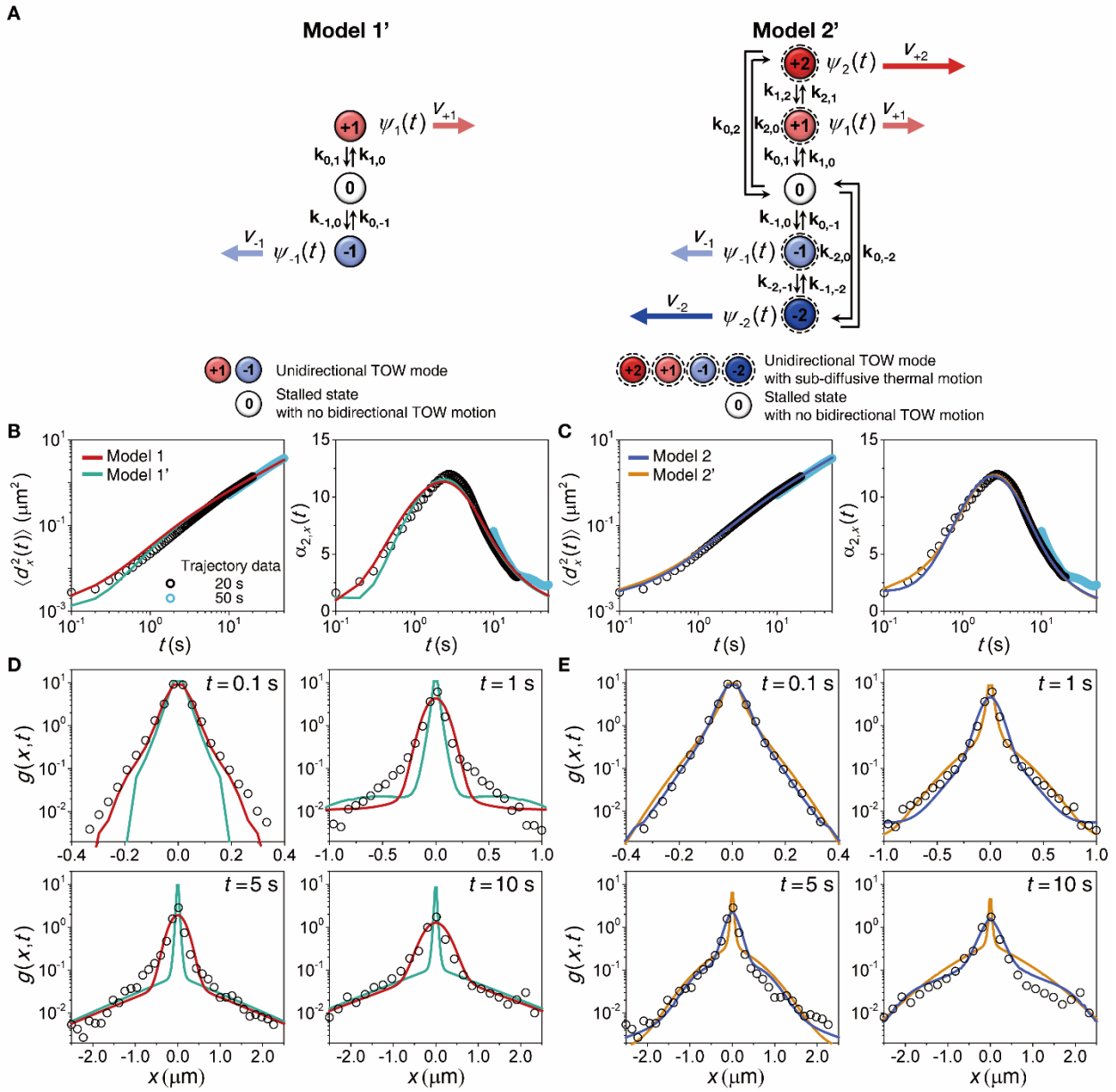

Figure S8. Variants of Model 1 and Model 2 compared against experimental results. (a) Schematic representations of Model 1′ and Model 2′, which are the simplified versions of Model 1 and Model 2 shown in Figure 2A. In each model, there exists no bidirectional active motion of the motor protein multiplex along the microtubule at state 0. For a detailed explanation of each model, see Method 2, Section 1. (B), (C) MSD and NGP of cargo displacement. (circles) Experimental results, (red and green lines) best fitted results of Model 1 and Model 1′, (blue and

yellow lines) best fitted results of Model 2 and Model 2′. (D), (E) Distribution of cargo displacement along the microtubule at various times. (circles) Experimental results, (red and green lines) predictions of Model 1 and Model 1′ best fitted to the MSD and NGP data, (blue and yellow lines) predictions of Model 2 and Model 2′ best fitted to the MSD and NGP data.

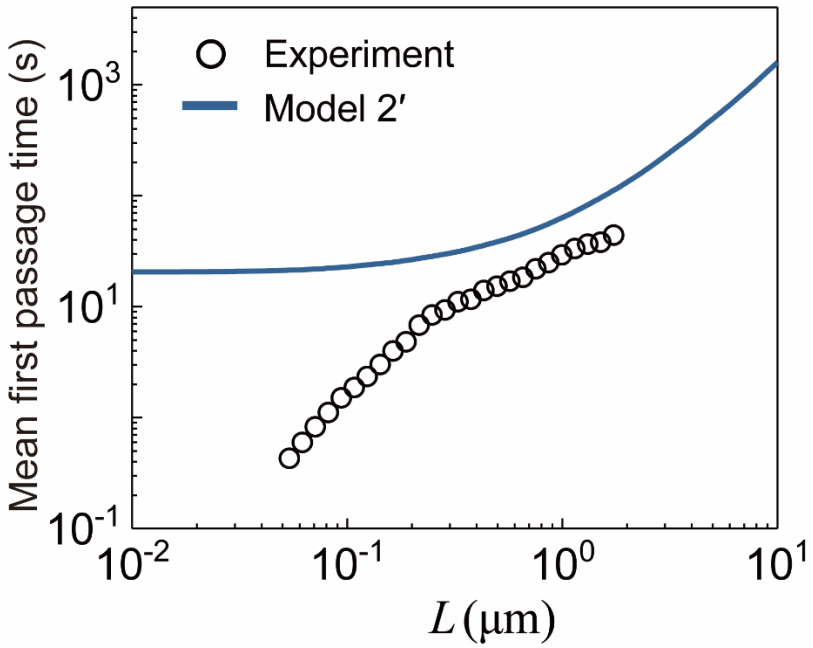

Figure S9. Comparison between result of Model 2′ and experimental data for the mean first passage time. Model 2′ in which the bidirectional active motion of the motor protein multiplex in Model 2 is neglected (see Figure S8). When optimized against experimental data, Model 2′ as well can provide a quantitative explanation of the MSD and NGP as shown in Figure S8. However, in contrast with Model 2, Model 2′ cannot explain diffusive scaling of the MFPT at short travel lengths or transitions of the MFPT from diffusive to ballistic scaling behavior, which are observed in experiment.

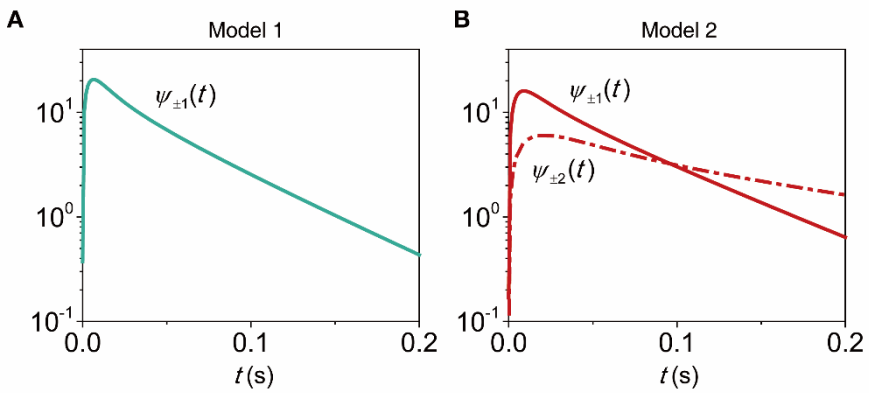

Figure S10. Waiting time distributions associated with ATP-hydrolysis coupled unidirectional motion. (A), (B) Distributions, $\psi_i(t)$, of time elapsed for the motor protein multiplex at the *i*th mode to perform ATP-hydrolysis coupled transport from one site to one-of-two adjacent sites along the microtubule for Model 1 and Model 2. These distributions are extracted by comparing Model 1 and Model 2 with experimental results of the mean square displacement and non-Gaussian parameter of *in vivo* vesicles.

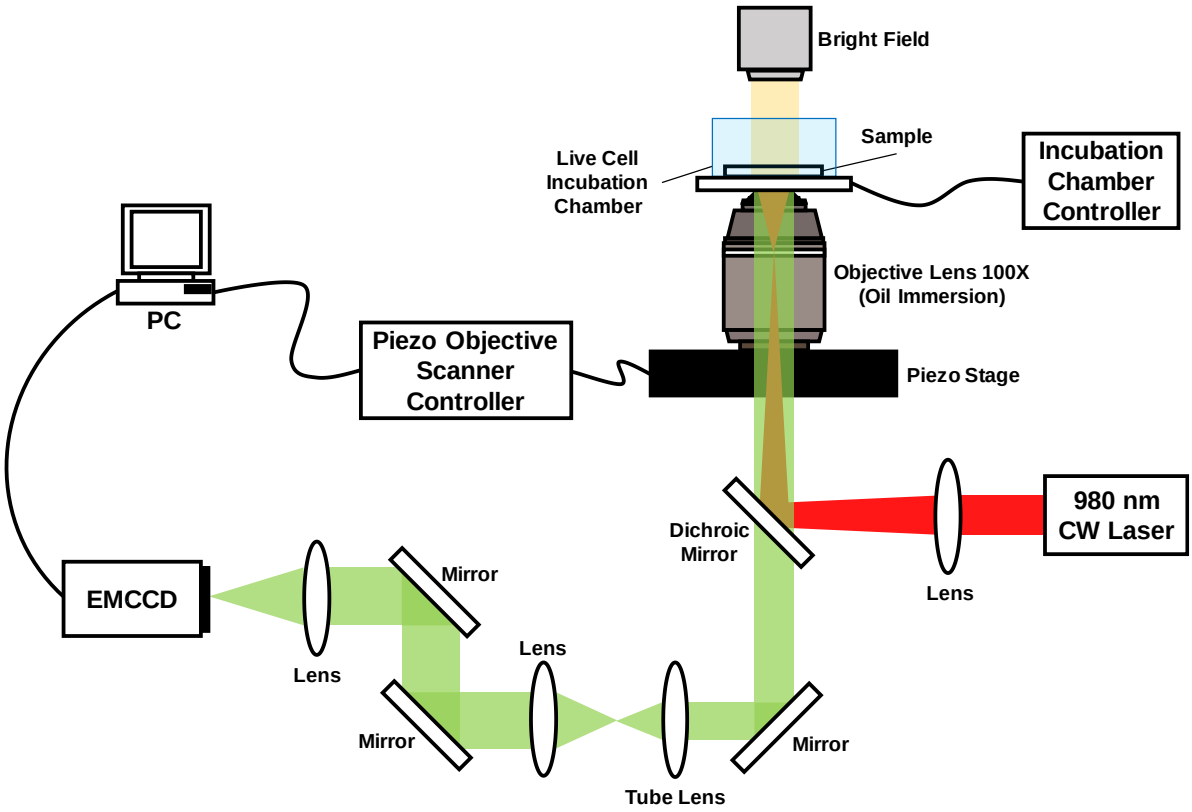

Figure S11. Schematic diagram of experimental set-up.

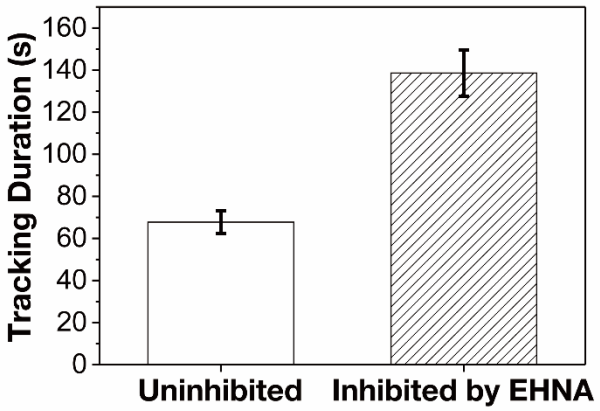

Figure S12. Mean trajectory length of UCNP cargo in untreated and EHNA-treated cells. Average tracking duration in uninhibited and dynein-inhibited cells were 67.74 ± 5.471 and 138.6 ± 10.98 s, respectively.

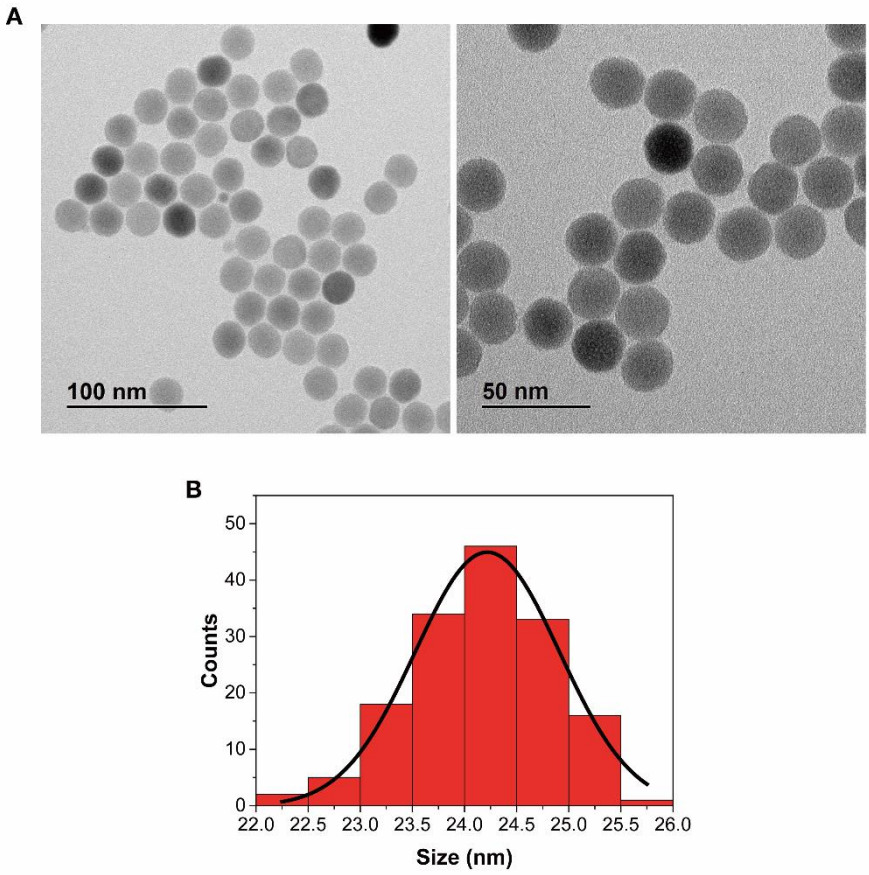

Figure S13. TEM images and size distribution of synthesized UCNPs. (A) TEM images of core UCNPs. (B) Size distribution of UCNPs (from 155 single core UCNPs). The average diameter of UCNPs, which was obtained from the Gaussian curve (black) for the size distribution, was 24.2 ± 0.7 nm (mean ± standard deviation).

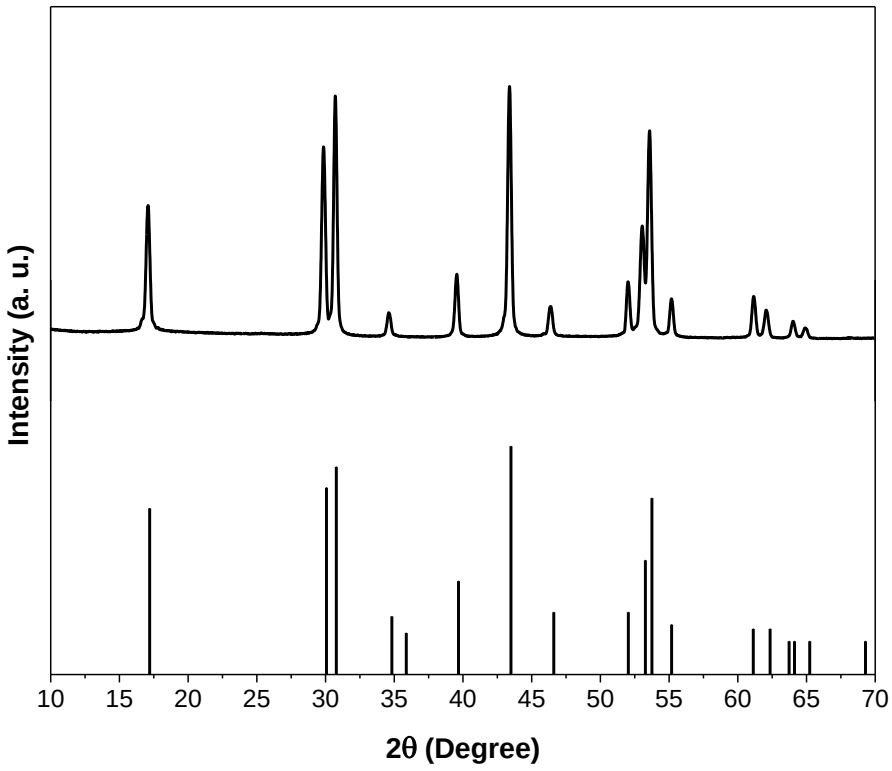

Figure S14. XRD data of synthesized UCNPs. Obtained XRD pattern of UCNPs is the same as that of previously reported hexagonal phase UCNPs.

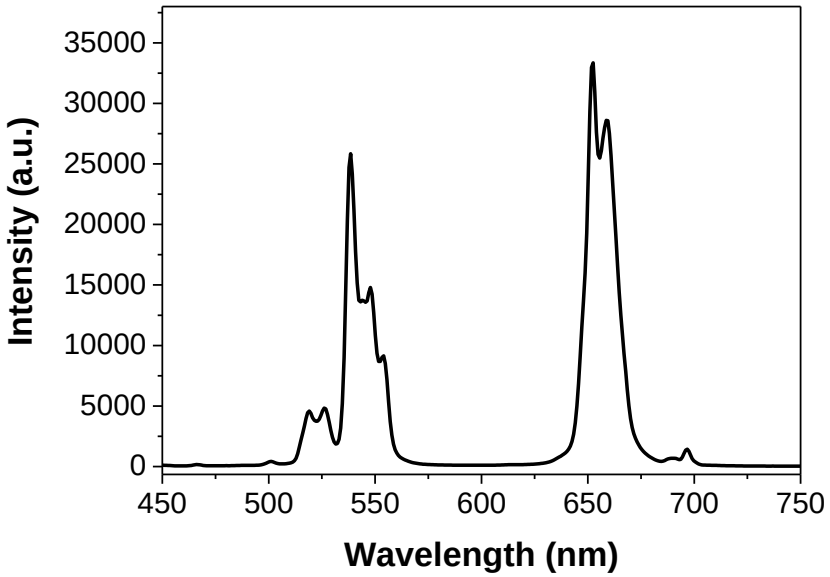

Figure S15. Emission spectrum of UCNPs. $NaYF_4$: Yb^{3+}, Er^{3+} UCNPs were excited by a 980 nm laser and emitted green (525 and 545 nm) and red (655 nm) photons.

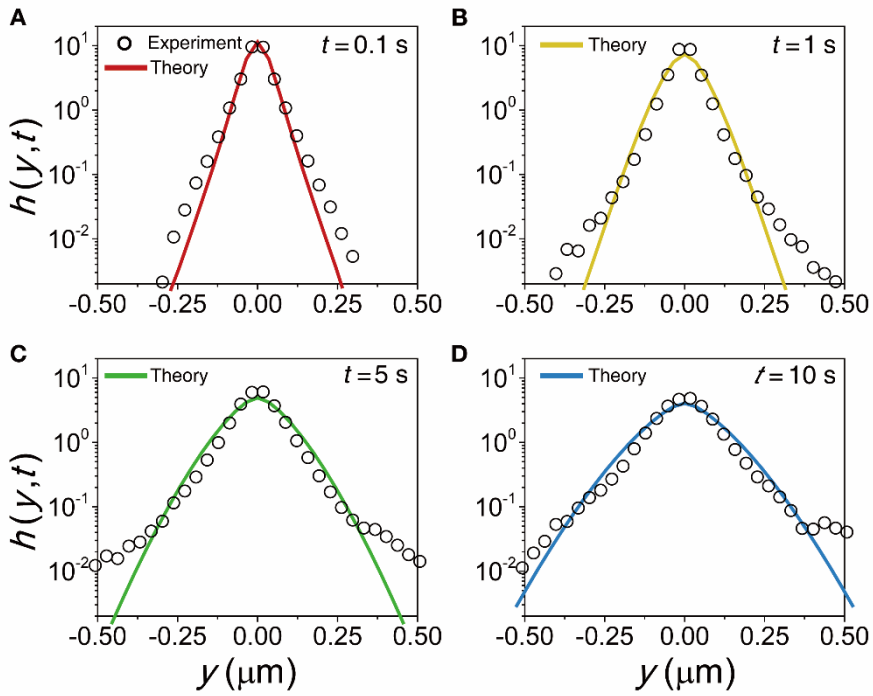

Figure S16. Distribution of cargo displacement in the microtubule-orthogonal direction. Distribution, $h(y,t)$, of cargo displacement in the microtubule-orthogonal direction at various times. (circles) Experimental results, (lines) theoretical results [eq M0-58].

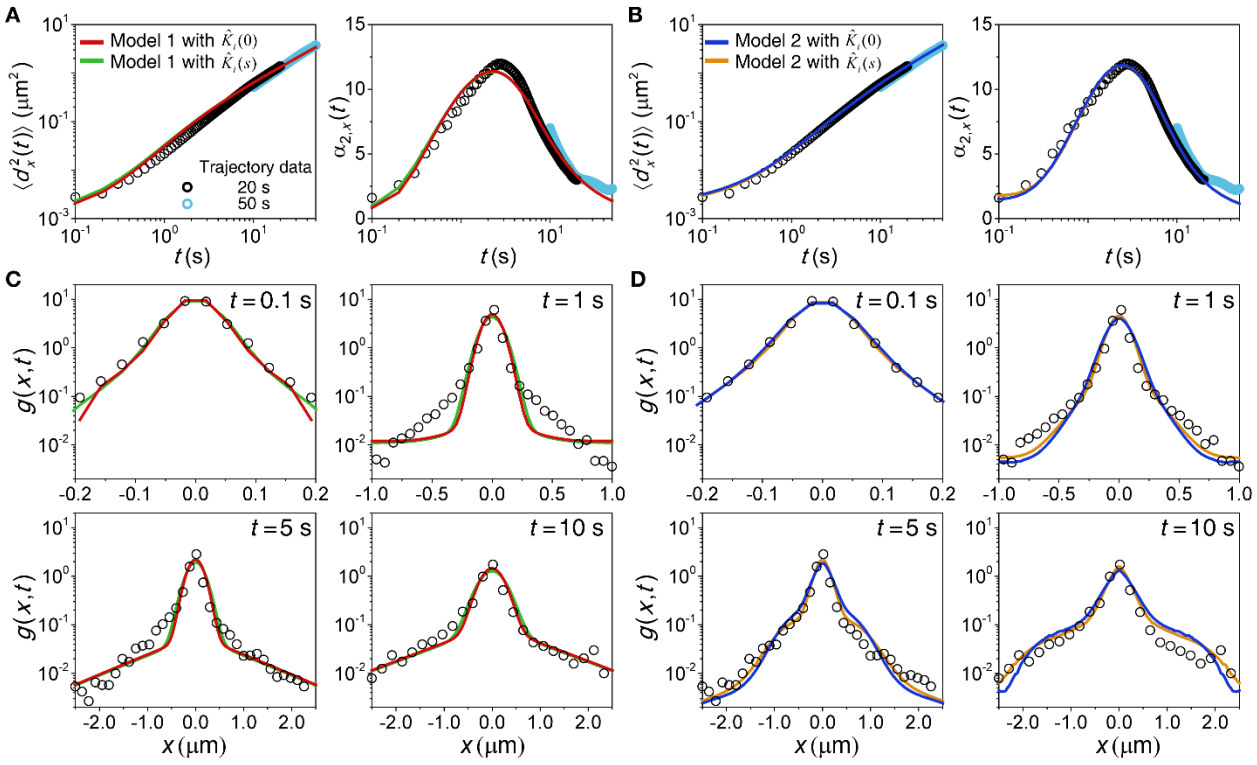

Figure S17. Comparison between two different approaches for the drift kernel. Model 1 and Model 2 using the small-s limit, $v_i = \left[\hat{K}_i(s=0)\right]$, of $\hat{K}_i(s)$ in eqs M0-33 and M0-38 are respectively compared with Model 1 and Model 2 using $\hat{K}_i(s)$ given by the second formula in eq M0-27 instead of $\hat{K}_i(0)$ (see Method 2). (A), (B) MSD and NGP of cargo displacement. (circles) Experimental results, (red and green lines) best fitted results of Model 1 with $\hat{K}_i(0)$ and Model 1 with $\hat{K}_i(s)$, (blue and yellow lines) best fitted results of Model 2 with $\hat{K}_i(0)$ and Model 2 with $\hat{K}_i(s)$. (C), (D) Distribution of cargo displacement along the microtubule at various times. (circles) Experimental results, (red and green lines) predictions of Model 1 with $\hat{K}_i(0)$ and Model 1 with $\hat{K}_i(s)$ best fitted to the MSD and NGP data, (blue and yellow lines) predictions of Model 2 with $\hat{K}_i(0)$ and Model 2 with $\hat{K}_i(s)$ best fitted to the MSD and NGP data.

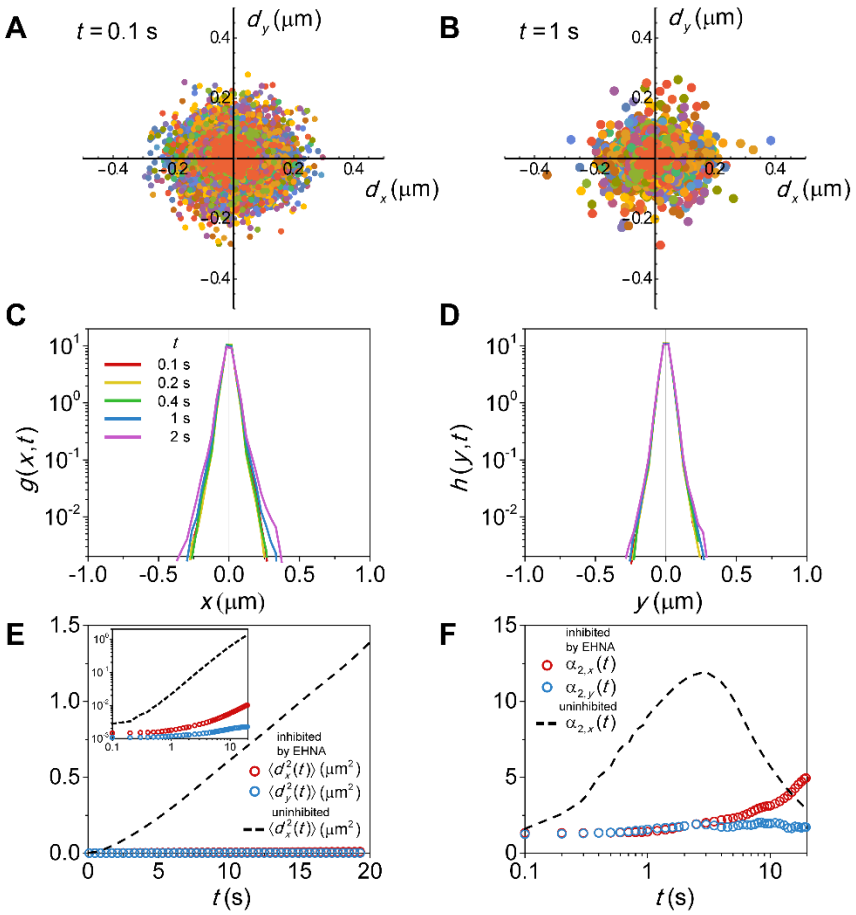

Figure S18. UCNP cargo displacement distribution and moments after dynein inhibition by EHNA. (A), (B) Two-dimensional representation of the displacement trajectories when the measurement times are 0.1 second and 1 second. (C) Cargo displacement distribution in the microtubule direction at various times. (D) Cargo displacement distribution in the microtubule-orthogonal direction. Both distributions show marginal time dependence. (E) The MSD in the microtubule direction (red circles). The MSD in the microtubule-orthogonal direction (blue circles). Both are negligible compared to the MSD in the absence of dynein inhibition (dotted line). The inset represents the log-log plot of the same figure. (F) The non-Gaussian parameter of the cargo displacement in the microtubule direction (red circles). The non-Gaussian parameter of cargo displacement in the microtubule-orthogonal direction (blue circles).

SUPPLEMENTARY TABLES

Table S1. ICP-MS data of synthesized UCNPs. The ratios of lanthanide ions were Y: 78.573 %, Yb: 19.276 %, and Er: 2.151 %.

	Y	**Yb**	**Er**
Composition ratio (%)	78.57332	19.27564	2.15104

Table S2. Optimized values of the adjustable parameters that achieve quantitative explanation of cargo motion dynamics in the microtubule-orthogonal direction. D_y^a and a are two parameters characterizing the fractional diffusion kernel given by eq M0-61.

Adjustable parameters	**Values**
Parameters characterizing fractional diffusion in the microtubule-orthogonal direction	
D_y^a	1.19×10^{-3} $\mu m^2/s^a$
a	0.69

CAPTIONS FOR SUPPLEMENTARY MOVIES

Movie S1. Time-lapse movie of intracellular transport of UCNPs in SH-SY5Y cell. UCNP cargo transport in an SH-SY5Y cell is shown. We used Diatrack software, to obtain a dataset of trajectories at temporal and spatial resolution of 10 fps (for 300 s) and 0.101 μm, respectively.

Movie S2. Time-lapse movie of intracellular transport of UCNPs in dynein-inhibited SH-SY5Y cell. UCNP cargo transport in a dynein-inhibited SH-SY5Y cell is shown in this movie. Most UCNPs are stationary during our observation time.

SUPPLEMENTARY REFERENCES

1. Jo, H. L.; Song, Y. H.; Park, J.; Jo, E. J.; Goh, Y.; Shin, K.; Kim, M. G.; Lee, K. T., Fast and background-free three-dimensional (3D) live-cell imaging with lanthanide-doped upconverting nanoparticles. *Nanoscale* **2015,** *7* (46), 19397-402.

2. Thompson, R. E.; Larson, D. R.; Webb, W. W., Precise nanometer localization analysis for individual fluorescent probes. *Biophys. J.* **2002,** *82* (5), 2775-2783.

3. Deschout, H.; Zanacchi, F. C.; Mlodzianoski, M.; Diaspro, A.; Bewersdorf, J.; Hess, S. T.; Braeckmans, K., Precisely and accurately localizing single emitters in fluorescence microscopy. *Nat. Methods* **2014,** *11* (3), 253-266.

4. Park, Y.; Kim, H. M.; Kim, J. H.; Moon, K. C.; Yoo, B.; Lee, K. T.; Lee, N.; Choi, Y.; Park, W.; Ling, D.; Na, K.; Moon, W. K.; Choi, S. H.; Park, H. S.; Yoon, S. Y.; Suh, Y. D.; Lee, S. H.; Hyeon, T., Theranostic Probe Based on Lanthanide-Doped Nanoparticles for Simultaneous In Vivo Dual-Modal Imaging and Photodynamic Therapy. *Adv. Mater.* **2012,** *24* (42), 5755-5761.

5. Park, S. J.; Song, S.; Jeong, I.-C.; Koh, H. R.; Kim, J.-H.; Sung, J., Nonclassical Kinetics of Clonal yet Heterogeneous Enzymes. *J. Phys. Chem. Lett.* **2017,** *8* (13), 3152-3158.

6. Shim, J. U.; Ranasinghe, R. T.; Smith, C. A.; Ibrahim, S. M.; Hollfelder, F.; Huck, W. T. S.; Klenerman, D.; Abell, C., Ultrarapid Generation of Femtoliter Microfluidic Droplets for Single-Molecule-Counting Immunoassays. *Acs Nano* **2013,** *7* (7), 5955-5964.

7. Cox, D. R., *Renewal theory*. Methuen London: London,, 1967; Vol. 1.

8. Kenkre, V.; Montroll, E.; Shlesinger, M., Generalized master equations for continuous-time random walks. *J. Stat. Phys.* **1973,** *9* (1), 45-50.

9. Risken, H., *The Fokker-Planck equation*. 2nd ed.; Springer: 1996.

10. Yang, S.; Cao, J.; Silbey, R. J.; Sung, J., Quantitative Interpretation of the Randomness in Single Enzyme Turnover Times. *Biophys. J.* **2011,** *101* (3), 519-524.

11. Visscher, K.; Schnitzer, M. J.; Block, S. M., Single kinesin molecules studied with a molecular force clamp. *Nature* **1999,** *400* (6740), 184-189.

12. Magdziarz, M.; Weron, A.; Weron, K., Fractional Fokker-Planck dynamics: Stochastic representation and computer simulation. *Phys. Rev. E* **2007,** *75* (1), 016708.

13. Annunziato, M.; Borzì, A.; Magdziarz, M.; Weron, A., A fractional Fokker–Planck control framework for subdiffusion processes. *Optim. Control Appl. Methods* **2016,** *37* (2), 290-

304.

14. Kubo, R., The fluctuation-dissipation theorem. *Rep. Prog. Phys.* **1966,** *29* (1), 255.